



Divergent and Ultrahigh Thermal Conductivity in Millimeter-Long Nanotubes

Victor Lee,^{1,2} Chi-Hsun Wu,^{1,2} Zong-Xing Lou,^{1,2} Wei-Li Lee,³ and Chih-Wei Chang^{1,*}

¹*Center for Condensed Matter Sciences, National Taiwan University, Taipei 10617, Taiwan*

²*Department of Physics, National Taiwan University, Taipei 10617, Taiwan*

³*Institute of Physics, Academia Sinica, Taipei 11529, Taiwan*

(Received 15 December 2015; published 30 March 2017)

Low-dimensional materials could display anomalous thermal conduction that the thermal conductivity (κ) diverges with increasing lengths, in ways inconceivable in any bulk materials. However, previous theoretical or experimental investigations were plagued with many finite-size effects, rendering the results either indirect or inconclusive. Indeed, investigations on the anomalous thermal conduction must demand the sample length to be sufficiently long so that the phenomena could emerge from unwanted finite-size effects. Here we report experimental observations that the κ 's of single-wall carbon nanotubes continuously increase with their lengths over 1 mm, reaching at least 8640 W/mK at room temperature. Remarkably, the anomalous thermal conduction persists even with the presence of defects, isotopic disorders, impurities, and surface adsorbates. Thus, we demonstrate that the anomalous thermal conduction in real materials can persist over much longer distances than previously thought. The finding would open new regimes for wave engineering of heat as well as manipulating phonons at macroscopic scales.

DOI: 10.1103/PhysRevLett.118.135901

The law of heat transfer in a solid was discovered by Fourier in 1811. Under the steady state, Fourier's law of heat conduction is expressed as

$$J = -\kappa \nabla T, \quad (1)$$

which explicitly states that the heat flux density (J) is proportional to the temperature gradient, and the proportional constant is the thermal conductivity (κ). Empirically, κ is often found to be a constant of a bulk material and is independent of sample geometries. Thus, Fourier's law, together with Ohm's law for electrical conduction and Fick's law for gas diffusion, are traditionally categorized as examples of normal diffusion phenomena.

On the other hand, continuous efforts in seeking solid theoretical grounds for the empirical results have pointed out that anomalous thermal conduction ($\kappa \sim L^\alpha$, $\alpha > 0$, where L is the sample length) could occur in low-dimensional systems [1]. These works, though sometimes referred to as non-Fourier thermal conduction (which, strictly speaking, only applies when the speed of heat conduction cannot be neglected), may be more appropriately described as violations of normal diffusion processes ($\alpha = 0$) in heat conduction. Theoretically, the divergence of κ in one-dimensional systems has been shown to be very robust against disorder or anharmonicity [2–5]. In many models, heat transfer phenomena would depend on the dimensionalities of the system, showing sublinear power-law ($\alpha < 1$) divergence in 1D [1], logarithmic divergence in 2D [6], and normal ($\alpha = 0$) thermal conduction in 3D [7,8]. Apart from the idealized models, it has been suggested that the anomalous thermal conduction could be observed in real systems like single-wall carbon nanotubes (CNTs) [9–17] or graphene ribbons [18]. For example, in a perfect

(i.e., isotopically pure and defect-free) CNT, its κ is predicted to increase sublinearly ($\alpha = 0.33 - 0.5$) with lengths up to millimeters [9,10], characteristically differing from conventional ballistic thermal conduction (i.e., $\alpha = 1$).

However, theoretical disputes on many anomalous effects have not been completely settled yet. For example, while the anomalous thermal conduction is commonplace in many 1D models [19,20], it remains controversial whether a quasi-1D system like a CNT would eventually restore back to normal thermal conduction at finite lengths [9–17]. Experimentally, the formidable challenges in fabricating nanomaterials with very high aspect ratios and the difficulties in measuring their κ 's, combined with unwanted finite-size effects such as fluctuations of defect or disorder densities or conventional ballistic thermal conduction pertinent to micron-sized samples, have plagued many previous experimental observations [21–25].

To rigorously study the fundamental heat transfer phenomena, experimental investigations should be conducted on sufficiently long CNTs. We thus synthesized ultralong single-wall CNTs with lengths exceeding 2 cm using chemical vapor deposition methods [26]. Individual CNTs were picked up by a tailored manipulator and placed on a thermal conductivity test fixture consisting of parallel suspended SiN_x beams, as shown in Fig. 1(a). The suspended SiN_x beams with deposited Pt films were utilized as independent resistive thermometers (RTs) for generating heat or sensing temperature variations. For example, if a Joule heating power (P) is injected at RT_1 [Fig. 1(b)], most of the power will dissipate along RT_1 to the heat bath, following $P_1 = 8\Delta T_1/R_{b1}$ (where R_{b1} is the total thermal resistance of the RT_1 and ΔT_1 is the temperature rise above

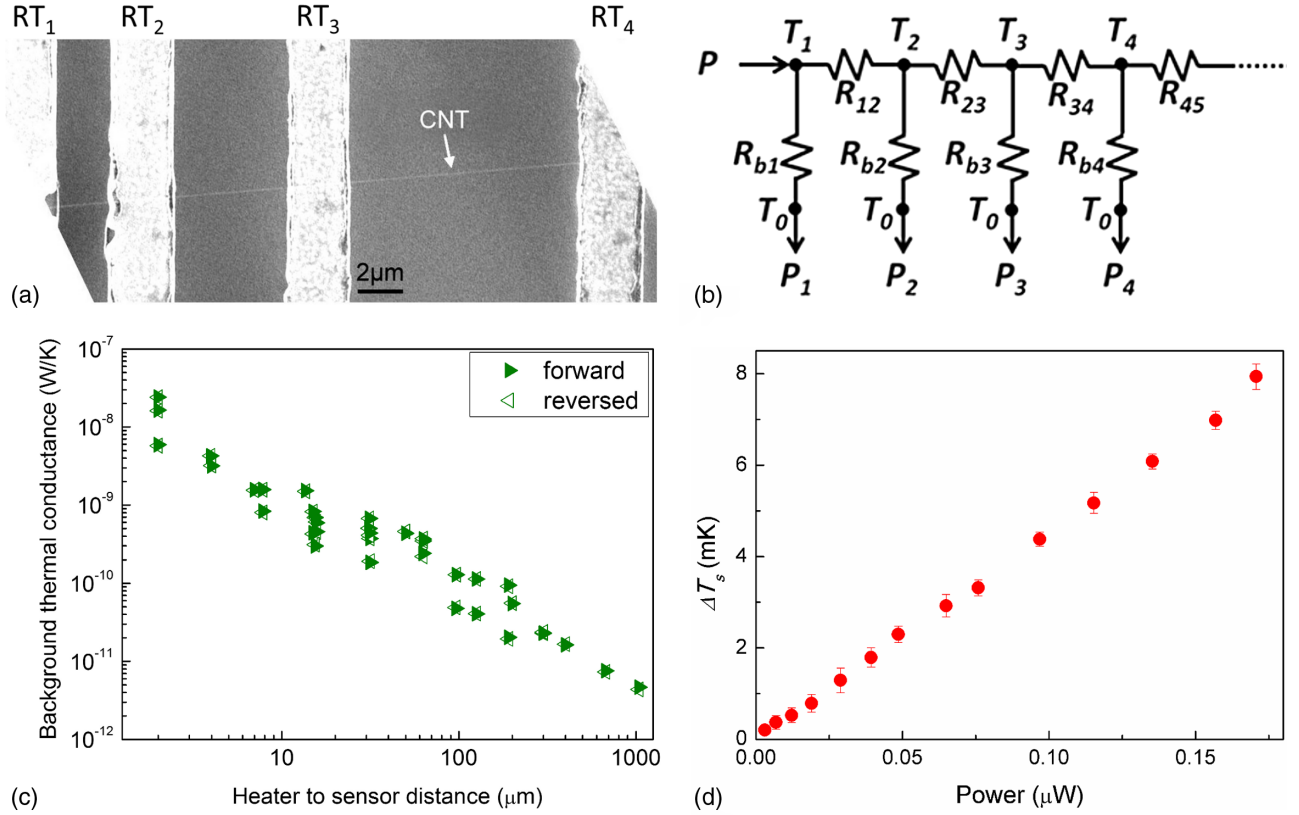


FIG. 1. (a) SEM image of a CNT anchored on a test fixture consisting of parallel resistive thermometers (RT_i 's) made by Pt films on SiN_x beams. (b) The corresponding thermal circuits when RT_1 is used as a heater. (c) Measured background thermal conductance due to radiation heat transfer (from heater to sensor) for various heater-to-sensor distances. The measured values for forward and reversed biases (i.e., exchanging the role of the heater and the sensor) are shown, demonstrating $f_{ij} = 1 \pm 0.04$. We have noticed that the background thermal conductance is sensitive to the environment (such as whether the Si substrate is fully etched through or partially etched), so that the measured values are different even if the heater-to-sensor distances are similar. (d) Measure ΔT_s vs P for driving frequency at 2 Hz, which gives a noise equivalent thermal conductance of $4.7 \times 10^{-12} \text{ W K}^{-1} \text{ Hz}^{-1/2}$ at room temperature.

the heat bath, measured at the middle of RT_1 , where a CNT is anchored). On the other hand, the power flowing through the CNT is the sum of the power measured by individual sensors; i.e., $P_j = 4\Delta T_j/R_{bj}$. Because $P = P_1 + P_2 + P_3 + \dots$, the thermal conductance of the CNT (K_{12}) anchored between RT_1 and RT_2 follows

$$K_{12} = \frac{4\left(\frac{\Delta T_2}{R_{b2}} + \frac{\Delta T_3}{R_{b3}} + \dots\right)}{\Delta T_1 - \Delta T_2} = \frac{P(f_{12}\Delta T_2 + f_{13}\Delta T_3 + \dots)}{(2\Delta T_1 + f_{12}\Delta T_2 + f_{13}\Delta T_3 + \dots)(\Delta T_1 - \Delta T_2)}, \quad (2)$$

where $f_{ij} \equiv R_{bi}/R_{bj}$. The f_{ij} 's can be determined from the asymmetry of background measurement before anchoring a CNT. As shown in Fig. 1(c), we have found that although the measured background thermal conductances varied from $3.18 \times 10^{-9} \text{ W/K}$ to $4.51 \times 10^{-12} \text{ W/K}$ (for heater-to-sensor distance $4 \mu\text{m} - 1.039 \text{ mm}$), they display symmetric results; i.e., $f_{ij} = 1 \pm 0.04$. In addition, the temperature rise of the heater (sensor) is a parabolic (linear) function of the location; thus, we have $\overline{\Delta T} = 2\Delta T_1/3$ and $\overline{\Delta T}_j = \Delta T_j/2$

(where $j = 2, 3, 4, \dots$ and $\overline{\Delta T}_i$ is the average temperature rise of RT_i) [26]. Experimentally, we have found that $\overline{\Delta T}_1 \sim 20 \text{ K} \gg \overline{\Delta T}_2 \gg \overline{\Delta T}_3 \gg \overline{\Delta T}_4$. Thus, the thermal conductance (K_{12}) of a CNT anchored between RT_1 and RT_2 can be expressed by

$$K_{12} = \frac{2P(\overline{\Delta T}_2 + \overline{\Delta T}_3 + \dots)}{3\overline{\Delta T}_1 \left(\frac{3}{2}\overline{\Delta T}_1 - \overline{\Delta T}_2 \right)}. \quad (3)$$

The above result can be generalized to thermal conductance of a CNT anchored between any neighboring RT_i and RT_j . During the experiment, an alternating current with frequency f ($< 7 \text{ Hz}$) was supplied to the heater (RT_i) and the corresponding changes of the temperature on the sensor (RT_j) were detected at frequency $2f$ using a lock-in amplifier. The background contribution due to radiation heat transfer from the heater to the sensor had been carefully measured and subtracted so as to obtain the thermal conductance of the CNTs on the same device and of identical heater-sensor configurations. As shown in Fig. 1(d), the test fixture is capable of measuring temperature variations

~ 0.28 mK at room temperature (time constant = 10 sec), which is equivalent to a thermal conductance resolution 4.7×10^{-12} WK $^{-1}$ Hz $^{-1/2}$. After the measurement, sections of sample 6 and sample 9 were successfully transferred to a TEM for further characterizations [26]. Unfortunately, due to the vibrations of the long CNTs under TEM imaging, the diameter (d) cannot be precisely measured. We thus assume $d = 2$ nm and thickness $\delta = 0.34$ nm for determining the measured $\kappa_m = KL/\pi d\delta$ of the investigated CNTs. Importantly, the investigated L 's span from few micrometers [Fig. 1(a)] to millimeters (Fig. 2; see also Ref. [26] for SEM images of the investigated CNTs).

Figure 3 shows κ_m vs L relations for nine different CNTs. The L 's of the investigated CNTs span 3 orders of magnitude, varying from 2 μ m to 1.039 mm. Because the diameter and the chirality are less likely to change in an ultralong CNT [27], the uncertainties can be minimized by analyzing the length dependence of κ of the same sample. Remarkably, the measured κ_m 's (open symbols) of sample 2 to sample 9 display unambiguous divergent behavior with increasing L . No divergence of κ_m is observed in sample 1, possibly due to



FIG. 2. SEM panorama of sample 9 (divided into three parts), where a CNT is suspended across a heater and a sensor (the horizontal beams in the top right and the bottom left images). The total suspended length of sample 9 is 1.039 mm. The arrows in the figures denote the CNT.

its relatively short L (< 30 μ m). For the longest CNT ($L = 1.039$ mm), $\kappa_m = 8638 \pm 734$ W/mK is measured (assuming $d = 2$ nm). Note that the effects of radiation heat loss from the CNT and contact thermal resistance have not been taken into account yet. Thus, $\kappa_m = 8638$ W/mK is a lower bound for the millimeter-long CNT.

Because of the radiation heat loss from the surface of the ultralong CNTs, the power received by the sensor is always smaller than that transmitted from the heater. Thus, the measured κ_m 's simply set the lower bound of the actual values. Moreover, because corrections from the radiation heat loss become more significant for longer L , they further enhance the divergent behavior of κ for ultralong CNTs [26]. We have analyzed the contribution of radiation heat loss and plotted the corrected values of κ 's. The divergent behavior is quantified using $\kappa \sim L^\alpha$. The α 's seem to vary from 0.1 to 0.5. However, for sample 6 ($L > 400$ μ m), sample 7 ($L > 400$ μ m), sample 8 ($L > 670$ μ m), and sample 9 ($L > 1$ mm) they are investigated over much larger length scales and may be closer to an ideal, disordered, quasi-1D system. Interestingly, their α 's are found to be 0.2–0.5, falling within theoretical predictions [9,13,14]. Notably, these α 's are smaller than previous results determined by micron-long, multiwall CNTs ($\alpha = 0.6$ –0.8) [23], indicating that the previous observation was mixed with conventional ballistic thermal conduction ($\alpha = 1$) of microscopic lengths. Note that after corrections from the radiation heat loss, the highest κ (assuming $d = 2$ nm) now respectively reaches 6900 W/mK for sample 5 ($L > 300$ μ m), 10 050 W/mK for sample 8 ($L > 670$ μ m), and 13 300 W/mK for sample 9 ($L > 1$ mm).

We now analyze the effect of contact thermal resistance. Because the contact areas ($\sim dw$, where d is the diameter of the CNT and $w = 2$ μ m is the width of a SiN $_x$ beam) between the CNT and each RT $_i$ are nearly identical for each sample, the contact thermal resistance ($1/K_c$) should be approximately a constant for individual CNTs and its effect can be analyzed in terms of a dimensionless quantity K_s/K_c , where K_s is the intrinsic thermal conductance of a 1 μ m-long CNT. So the measured thermal resistance ($1/K_m$) follows $1/K = (L/L_0)^{1-\alpha}/K_s + 1/K_c$, and the measured κ_m is expressed as

$$\kappa_m = \frac{K_s L}{\pi ds} \left(\frac{1}{(L/L_0)^{1-\alpha} + K_s/K_c} \right). \quad (4)$$

Here, $L_0 = 1$ μ m. To investigate the effect of the contact thermal resistance, we first assume that the CNT is an ordinary diffusive thermal conductor (i.e., $\alpha = 0$) and plot the result for different K_s/K_c 's in Fig. 4. From Fig. 4, it can be seen that although contact thermal resistance may yield spurious divergent behavior at short lengths, the curves always become flat for large L . Thus, the contact thermal resistance cannot explain the experimental data. Because the experimentally investigated L 's span 3 orders of magnitude yet the contact area remains the same, we

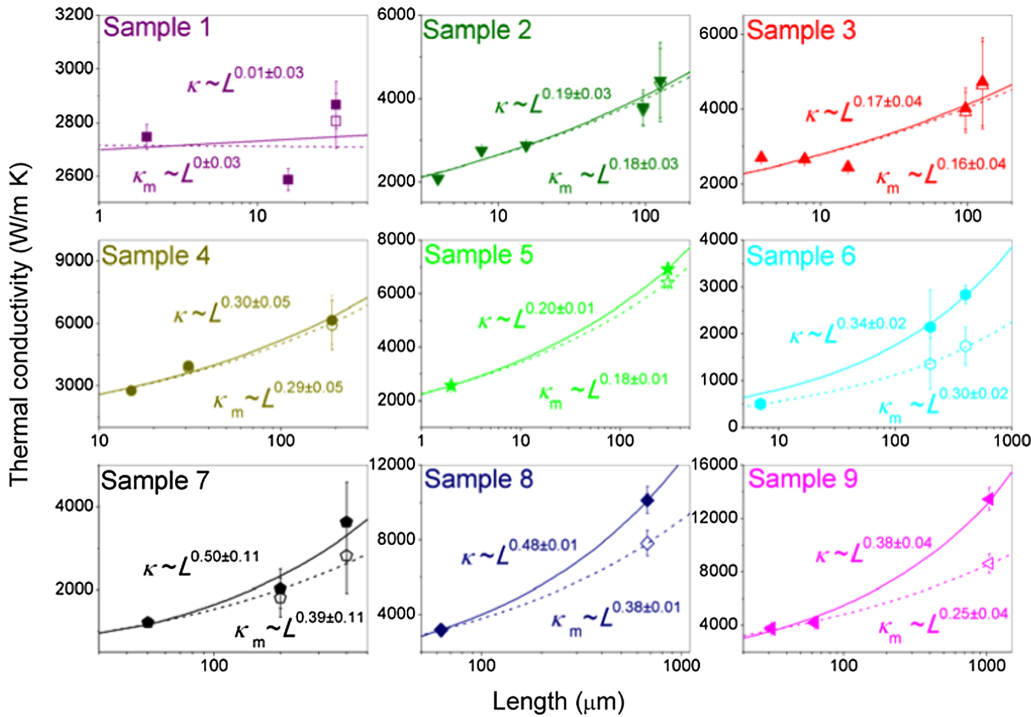


FIG. 3. κ vs L relations for nine different CNTs. Both measured κ_m 's (open symbols) and corrected κ 's (solid symbols, after incorporating radiation heat loss from the surface of CNTs) are shown for each sample. The measured κ_m 's and corrected κ 's are almost identical for $L < 100 \mu\text{m}$. For the longest CNT investigated ($L = 1.039 \text{ mm}$), the measured κ_m and the corrected κ reach 8640 and 13300 W/mK, respectively. The fits (by parametrizing $\kappa \sim L^\alpha$) to the corrected κ 's and measured κ_m 's are shown by solid curves and dashed curves, respectively.

have $L^{1-\alpha} \gg K_s/K_c$ in Eq. (4) and the effect of contact thermal resistance vanishes when $L \gg 1 \mu\text{m}$. Additionally, the effect of contact thermal resistance should be limited; for example, $K_s/K_c > 5$ would indicate that the intrinsic κ of a $1 \mu\text{m}$ -long CNT is larger than 18000 W/mK, violating quantum mechanical constraints for a CNT [28,29]. Further analyses using Eq. (4) suggest that $0.17 < \alpha < 0.43$ and $K_s/K_c < 0.3$ yield good fits to the experimental data [26]. Figure 4 also shows a controlled experiment on a SiN_x beam displaying the expected diffusive thermal conduction, demonstrating the validities of our measurements and analyses. Therefore, we conclude that the experimentally observed divergent behavior of κ originates from the intrinsic properties of the ultralong CNTs, but not from artifacts of contact thermal resistance.

Because naturally abundant ethanol vapor was used as the synthetic source, isotopic impurities (98.9% ^{12}C and 1.1% ^{13}C) are expected in the investigated CNTs. In addition, impurities and defects are unavoidable for the ultralong CNTs. Furthermore, TEM images reveal a thin layer ($\sim 2 \text{ nm}$) of amorphous carbon covering some parts of the CNTs [26]. Surprisingly, the pronounced power-law divergence of κ emerges regardless of these structural imperfections and external perturbations. The result is consistent with 1D disordered models that show robust anomalous thermal conduction phenomena against defects or disorders [5]. But it disagrees with the prediction that the divergent behavior of κ would disappear when defects are introduced in CNTs [9,16]. We thus demonstrate that the divergence of κ persists for much longer distances than theoretically anticipated [9,10,16]. Our results also resolve the decade-long debate of whether the κ of a CNT would

continue to diverge or saturate for $L > 1 \mu\text{m}$ [11–17]. The finding indicates that the wave properties of heat can be transmitted for much longer distances than previously thought, and it highlights the important contributions of long-wavelength phonons in low-dimensional systems.

Unlike electrical conductivity of materials that can vary by more than 27 orders of magnitude from insulators to metals,

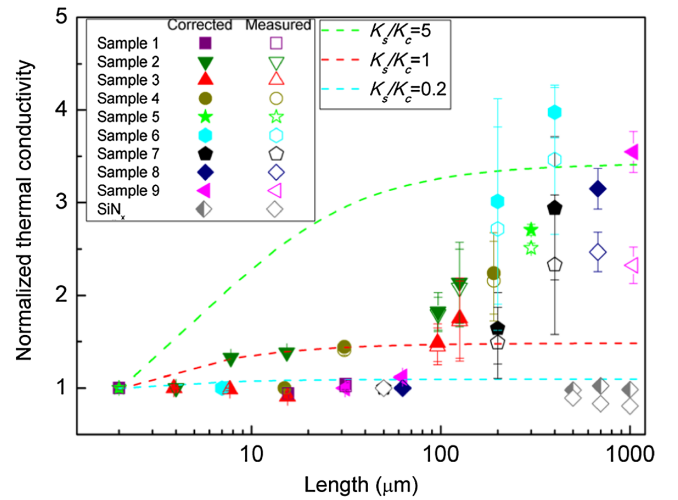


FIG. 4. Normalized κ vs L for the investigated samples. Here the corrected κ 's (solid symbols) and measured κ_m 's (open symbols) are normalized, respectively, by those of each sample's shortest L . The effects of contact thermal resistance from small ($K_s/K_c = 0.2$) to large ($K_s/K_c = 5$) are calculated using Eq. (4) (with $\alpha = 0$), demonstrating that the observed divergent of κ or κ_m cannot be attributed to contact thermal resistances adding to a diffusive thermal conductor. A controlled experiment on a SiN_x beam shows the expected normal thermal conduction.

κ 's were known to vary less than 10^5 from the best thermal conductors to the best thermal insulators in the past. The fundamental limitation has hampered most technological progress in directing heat or transmitting phonons. The divergent and ultrahigh κ observed in CNTs over 1-mm length scale could open a new domain for wave engineering of heat.

This work was supported by the Ministry of Science and Technology of Taiwan (MOST 104-2628-M-002-010-MY4).

V. L. and C.-H. W. contributed equally to this work.

*Corresponding author.

cwchang137@ntu.edu.tw

- [1] A. Dhar, *Adv. Phys.* **57**, 457 (2008).
- [2] K. Saito, S. Takesue, and S. Miyashita, *Phys. Rev. E* **54**, 2404 (1996).
- [3] S. Lepri, R. Livi, and A. Politi, *Phys. Rev. Lett.* **78**, 1896 (1997).
- [4] B. W. Li, H. Zhao, and B. B. Hu, *Phys. Rev. Lett.* **86**, 63 (2001).
- [5] A. Dhar and K. Saito, *Phys. Rev. E* **78**, 061136 (2008).
- [6] L. Yang, P. Grassberger, and B. Hu, *Phys. Rev. E* **74**, 062101 (2006).
- [7] K. Saito and A. Dhar, *Phys. Rev. Lett.* **104**, 040601 (2010).
- [8] L. Wang, D. He, and B. Hu, *Phys. Rev. Lett.* **105**, 160601 (2010).
- [9] N. Mingo and D. A. Broido, *Nano Lett.* **5**, 1221 (2005).
- [10] L. Lindsay, D. A. Broido, and N. Mingo, *Phys. Rev. B* **80**, 125407 (2009).
- [11] Z. H. Yao, J. S. Wang, B. W. Li, and G. R. Liu, *Phys. Rev. B* **71**, 085417 (2005).
- [12] D. Donadio and G. Galli, *Phys. Rev. Lett.* **99**, 255502 (2007).
- [13] G. Zhang and B. W. Li, *J. Chem. Phys.* **123**, 114714 (2005).
- [14] S. Maruyama, *Physica (Amsterdam)* **323B**, 193 (2002).
- [15] J. A. Thomas, R. M. Iutzi, and A. J. H. McGaughey, *Phys. Rev. B* **81**, 045413 (2010).
- [16] C. Sevik, H. Sevincli, G. Cuniberti, and T. Cagin, *Nano Lett.* **11**, 4971 (2011).
- [17] K. Saaskilanti, J. Oksanen, S. Volz, and J. Tulkki, *Phys. Rev. B* **91**, 115426 (2015).
- [18] D. L. Nika, A. S. Askerov, and A. A. Balandin, *Nano Lett.* **12**, 3238 (2012).
- [19] T. Prosen and D. K. Campbell, *Phys. Rev. Lett.* **84**, 2857 (2000).
- [20] T. Mai and O. Narayan, *Phys. Rev. E* **73**, 061202 (2006).
- [21] H. Hayashi, T. Ikuta, T. Nishiyama, and K. Takahashi, *J. Appl. Phys.* **113**, 014301 (2013).
- [22] H. Y. Chiu, V. V. Deshpande, H. W. C. Postma, C. N. Lau, C. Miko, L. Forro, and M. Bockrath, *Phys. Rev. Lett.* **95**, 226101 (2005).
- [23] C. W. Chang, D. Okawa, H. Garcia, A. Majumdar, and A. Zettl, *Phys. Rev. Lett.* **101**, 075903 (2008).
- [24] M. H. Bae, Z. Y. Li, Z. Aksamija, P. N. Martin, F. Xiong, Z. Y. Ong, I. Knezevic, and E. Pop, *Nat. Commun.* **4**, 1734 (2013).
- [25] X. F. Xu, L. F. C. Pereira, Y. Wang, J. Wu, K. W. Zhang, X. M. Zhao, S. Bae, C. T. Bui, R. G. Xie, J. T. L. Thong, B. H. Hong, K. P. Loh, D. Donadio, B. W. Li, and B. Ozyilmaz, *Nat. Commun.* **5**, 3689 (2014).
- [26] See Supplemental Material at <http://link.aps.org/supplemental/10.1103/PhysRevLett.118.135901>, which includes Refs. [27–35], for details of experimental methods and data analyses.
- [27] M. Hofmann, D. Nezich, A. Reina, and J. Kong, *Nano Lett.* **8**, 4122 (2008).
- [28] B. H. Hong, J. Y. Lee, T. Beetz, Y. M. Zhu, P. Kim, and K. S. Kim, *J. Am. Chem. Soc.* **127**, 15336 (2005).
- [29] S. M. Huang, X. Y. Cai, and J. Liu, *J. Am. Chem. Soc.* **125**, 5636 (2003).
- [30] L. X. Zheng, M. J. O'Connell, S. K. Doorn, X. Z. Liao, Y. H. Zhao, E. A. Akhadow, M. A. Hoffbauer, B. J. Roop, Q. X. Jia, R. C. Dye, D. E. Peterson, S. M. Huang, J. Liu, and Y. T. Zhu, *Nat. Mater.* **3**, 673 (2004).
- [31] T. L. Bergman, A. S. Lavine, and F. P. Incropera, *Fundamentals of Heat and Mass Transfer*, 7th ed. (Wiley, New York, 2011); M. Hofmann, D. Nezich, A. Reina, and J. Kong, *Nano Lett.* **8**, 4122 (2008).
- [32] T. K. Hsiao, H. K. Chang, S. C. Liou, M. W. Chu, S. C. Lee, and C. W. Chang, *Nat. Nanotechnol.* **8**, 534 (2013).
- [33] T. K. Hsiao, B. W. Huang, H. K. Chang, S. C. Liou, M. W. Chu, S. C. Lee, and C. W. Chang, *Phys. Rev. B* **91**, 035406 (2015).
- [34] R. Fainchtein, D. M. Brown, K. M. Siegrist, A. H. Monica, E. R. Hwang, S. D. Milner, and C. C. Davis, *Phys. Rev. B* **85**, 125432 (2012).
- [35] N. Mingo and D. A. Broido, *Phys. Rev. Lett.* **95**, 096105 (2005).

Supplemental Material for
Divergent and Ultrahigh Thermal Conductivity in Millimeter-Long Nanotubes

Victor Lee,^{1,2,†} Chi-Hsun Wu,^{1,2,†} Zong-Xing Lou,^{1,2} Wei-Li Lee,³ and Chih-Wei Chang^{1,*}

¹ Center for Condensed Matter Sciences, National Taiwan University, Taipei 10617, Taiwan

² Department of Physics, National Taiwan University, Taipei 10617, Taiwan

³ Institute of Physics, Academia Sinica, Taipei 11529, Taiwan

S1. Nanotube synthesis and device fabrication. High quality CNTs were grown using chemical vapor deposition (CVD) methods [1-4]. Solutions of 0.001 M FeCl₃ in water were used as catalysts. The CNTs were synthesized in a quartz tube within a furnace. First, the furnace was heated to 925°C under a flow of 1000 cm³/min Ar and 400 cm³/min H₂. Then Ar gas was directed through ethanol as the carbon source. The mixed Ar/ethanol and H₂ gases were flowed at 925°C for 20 minutes at the rates of 150 and 400 cm³/min, respectively. Finally, the furnace was cooled under a flow of 1000 cm³/min Ar and 400 cm³/min H₂. The resulting CNTs are found to exhibit lengths more than 2cm.

Figure S1 displays the schematic procedures of fabricating the thermal conductivity test fixtures. The device consists of several Pt/Cr (25 nm and 2 nm thick, respectively) resistive thermometer (RT) lines deposited on 2 μm wide, 500 nm thick, and 860 μm long SiN_x beams. First, Cr/Pt/Cr (50 nm, 25 nm, and 5 nm thick, respectively) metal lines and bonding pads were patterned using photolithography and electron-gun evaporation on a SiN_x/Si wafer (Fig. S1A and B). Then another photolithography was done to open a window in resist for dry etching. The unprotected region of SiN_x film was etched by inductively coupled plasma (ICP). The outermost Cr layers in metal lines were used to protect the underlying layers from ICP. The SiN_x beams together with metal lines were thus defined (Fig. S1C). The outermost Cr layers in metal lines were then removed by Cr-7t chromium etchant. Finally, the Si substrate in the window was etched through by aqueous KOH for transmission electron microscopy (TEM) characterizations (Fig. S1D). As shown in Fig. S2, the distances between neighboring beams vary from 2 μm to 1.039 mm, which allow thermal conductivity measurements on CNTs over very large length scales.

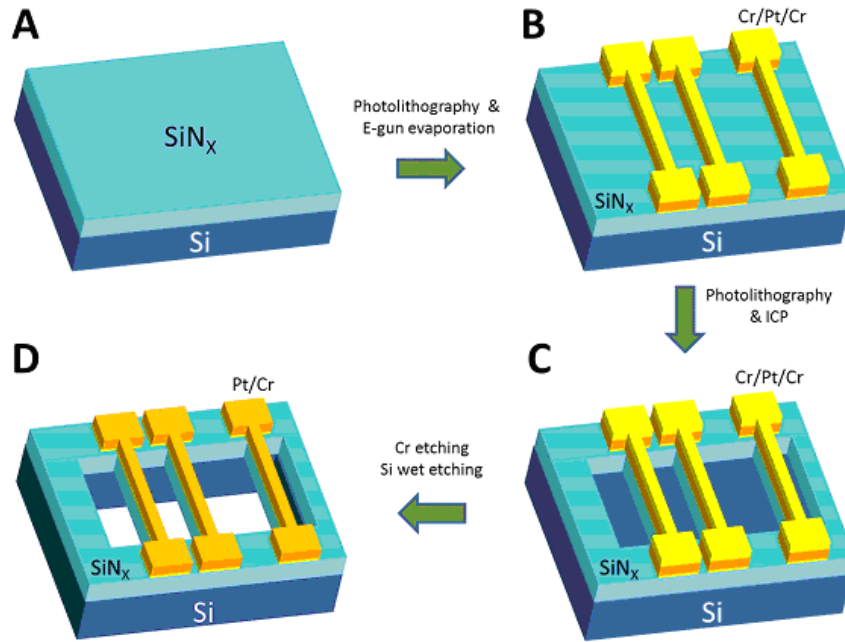


Fig. S1. Schematics of the fabrication procedures of the thermal conductivity test fixtures. (A and B) Cr/Pt/Cr metal lines were patterned using photolithography followed by electron-beam evaporation on a SiN_x/Si wafer. (C) Opening SiN_x windows by photolithography and ICP. (D) Etching away the topmost Cr layer and the bottom Si substrate.

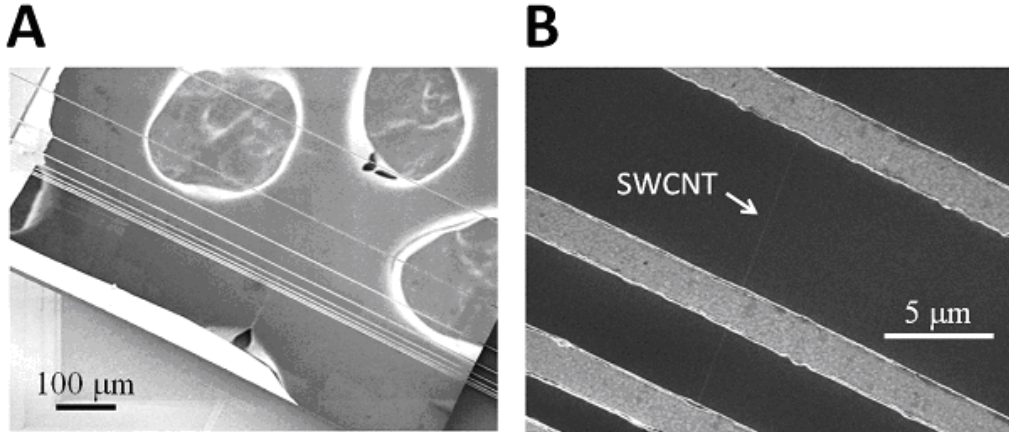


Fig. S2. (A) An SEM image of the fabricated thermal conductivity test fixture with the distances between neighboring heater/sensor varying from 2 μm to 1.039 mm. (B) An SEM image of an individual CNT suspending across several heaters/sensors.

S2. Thermal conductivity measurements. Figure S3A shows the schematic diagram of the thermal conductivity test fixture with an individual ultralong CNT suspended across several RT heater/sensor lines. The corresponding thermal circuit diagram is shown in Fig. S3B and C. When the leftmost RT line (RT₁) is heated (Fig. S3B), the temperature rise (ΔT_h) in RT₁ is a parabolic function of the location (x) on the RT₁

line[5], i.e.

$$\Delta T_h(x) \equiv T_h(x) - T_0 = -\frac{P}{4\kappa_{b1}LA}x^2 + C_1x + C_2 \quad (S1)$$

where $P = V_s^2/R_h$ is the Joule heating power, κ_{b1} is the effective thermal conductivity, L and A is respectively the half length and the cross section area of RT_1 . The constants C_1 and C_2 can be determined by the boundary condition

$$\Delta T_h(0) = \Delta T_h(2L) = 0 \quad (S2)$$

where $\Delta T_i = T_i - T_0$, and T_i is the temperature at the midpoint of RT_i ($i = 1, 2, 3, 4, \dots$), which are the RT lines shown in Fig. S3A. ΔT_h is then given by

$$\Delta T_h(x) = -\frac{P}{4\kappa_{b1}LA}x^2 + \frac{P}{2\kappa_{b1}A}x \quad (S3)$$

which gives

$$\Delta T_1 = \Delta T_h(L) = \frac{PL}{4\kappa_{b1}A} = \frac{P}{8}R_{b1} \quad (S4)$$

where $R_{bi} = 2L/\kappa_{bi}A$ is the total thermal resistance of the RT_i between T_i and the ambient heat sink. Based on energy conservation and the thermal resistance circuit shown in Fig. S3B, one can obtain

$$\frac{1}{R_{12}}(\Delta T_1 - \Delta T_2) = 4\left(\frac{\Delta T_2}{R_{b2}} + \frac{\Delta T_3}{R_{b3}} + \frac{\Delta T_4}{R_{b4}} + \dots\right) \quad (S5)$$

where R_{12} is the thermal resistance of the suspended segment of the CNT between RT_1 and RT_2 . One can thus get

$$K_{12} = \frac{4\left(\frac{\Delta T_2}{R_{b2}} + \frac{\Delta T_3}{R_{b3}} + \dots\right)}{\Delta T_1 - \Delta T_2} = \frac{4(f_{12}\Delta T_2 + f_{13}\Delta T_3 + \dots)}{R_{b1}(\Delta T_1 - \Delta T_2)} \quad (S6)$$

where $K_{12} \equiv 1/R_{12}$ is the sample thermal conductance and $f_{ij} \equiv R_{bi}/R_{bj}$, $i, j = 1, 2, 3, 4, \dots$. Because $P = P_1 + P_2 + P_3, \dots$ and from equations (S4) and (S6), one get

$$K_{12} = \frac{P(f_{12}\Delta T_2 + f_{13}\Delta T_3 + \dots)}{(2\Delta T_1 + f_{12}\Delta T_2 + f_{13}\Delta T_3, \dots)(\Delta T_1 - \Delta T_2)} = \frac{2P(f_{12}\overline{\Delta T_2} + f_{13}\overline{\Delta T_3} + \dots)}{3\overline{\Delta T_1}\left(\frac{3}{2}\overline{\Delta T_1} + (f_{12} - 2)\overline{\Delta T_2}\right)} \quad (S7)$$

where $\overline{\Delta T_i}$ ($i = 1, 2, 3, 4, \dots$) is the average temperature rise of each RT line. Due to the linear temperature profile in RT_2, RT_3, RT_4, \dots , $\Delta T_i = 2\overline{\Delta T_i}$ for $i = 2, 3, 4, \dots$

According to formula (S3), $\overline{\Delta T_1} = \frac{1}{L} \int_0^L \Delta T_1(x) dx = \frac{2}{3}\Delta T_1$. $\overline{\Delta T_i}$ can be obtained by measuring the increase in the electrical resistance of each RT line with the

temperature coefficient. The f_{ij} 's can be determined from the background measurement prior to that of the CNT. The background thermal conductance is due to radiation transfer and is symmetric when switching the role of heater and sensor (RT_1 and RT_2 here). We found that although the measured background thermal conductances (see Fig. S8) varied from 3.18×10^{-9} (heater to sensor distance = $4 \mu\text{m}$) to 4.51×10^{-12} W/K (heater to sensor distance = 1.039mm), they display symmetric results when exchanging the heater and the sensor. Thus we have $f_{ij} \sim 1$ and Eq. (S7) can be approximated to:

$$K_{12} = \frac{2P(\overline{\Delta T}_2 + \overline{\Delta T}_3 + \dots)}{3\overline{\Delta T}_1 \left(\frac{3}{2}\overline{\Delta T}_1 - \overline{\Delta T}_2 \right)} \quad (\text{S8})$$

We have also found that $\overline{\Delta T}_1 \sim 20\text{K} \gg \overline{\Delta T}_2 \gg \overline{\Delta T}_3 \gg \overline{\Delta T}_4$. Thus measuring $\overline{\Delta T}_1$ and $\overline{\Delta T}_2$ is sufficient to determine K_{12} . Due to the much smaller surface area of the CNT than that of the heater, the thermal radiation from the CNT itself is much smaller than the background contribution and can be ignored. In addition, we can also measure K_{21} by using RT_2 as the heater and RT_1 as the sensor (Fig. S3C). The corresponding formula can be obtained by similar methods. Likewise, the thermal resistance of other suspended CNT segment (R_{23} , R_{34} , $R_{45} \dots$) can be obtained by heating RT_2 , RT_3 , $RT_4 \dots$ and measuring the temperature rise of the neighboring RTs.

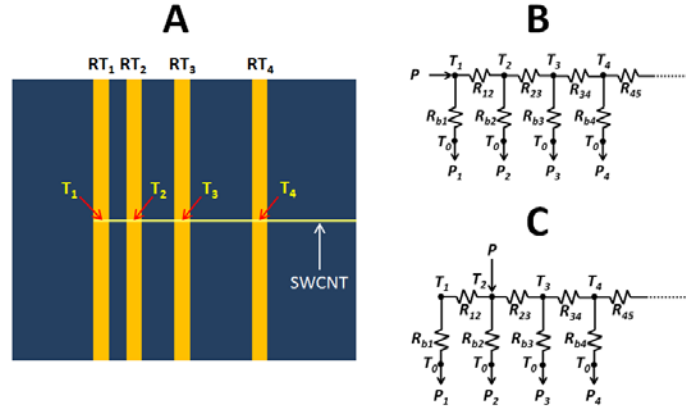


Fig. S3. (A) Schematic of the thermal conductivity test fixture consisting of parallel resistive thermometers. (B and C) The corresponding thermal circuits when (B) RT_1 or (C) RT_2 is used as a heater.

From Eq. (S8), we learn that the sample thermal conductance can be determined after measuring the Joule heating power (P) and temperature variations (ΔT_h for heaters and ΔT_s for sensors) of the RTs. Due to the linear relation of the resistance change (ΔR) with respect to the temperature change (ΔT) of the Pt resistors (Fig. S4):

$$\Delta R = c\Delta T \quad (S9)$$

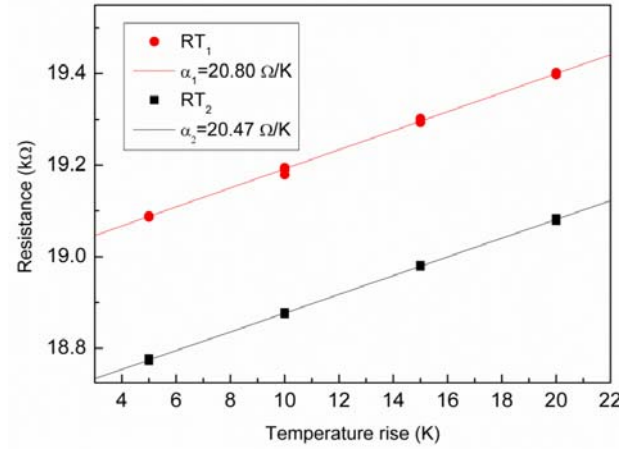


Fig. S4. Measured electrical resistances of the RT lines vs. the temperature rise.

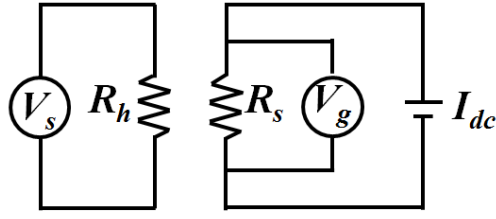


Fig. S5. Experimental schematic for applying an AC voltage (with angular frequency ω) to the heater resistance R_h and measuring the corresponding sensor resistance (R_s) variations at angular frequency 2ω .

(where c is the temperature coefficient), ΔT_h and ΔT_s can be directly obtained from the measuring the resistance variations of the heater (ΔR_h) and the sensor (ΔR_s). To achieve high sensitivity, we have developed a 2ω method for measuring the small variations of ΔR_s . As shown in Fig. S5, when an alternate voltage source V_s with angular frequency ω is applied to the heater, the temperature of the sensor follows:

$$T_s = T_0 + \Delta T_s \sin^2 \omega t \quad (S10)$$

where T_0 is the environmental temperature and ω is the frequency of the driven AC voltage. The voltage of the sensor is then given by

$$V = const. + \Delta V \sin^2 \omega t = const. - \frac{\Delta V}{2} \cos 2\omega t \quad (S11)$$

So when a small dc current $I_{dc} = 1\mu\text{A}$ is supplied to the sensor and the second-harmonic amplitude ($V_g(2\omega)$) is measured by a lock-in amplifier (Stanford Research 830), we have

$$V_g = \left| \frac{\Delta V}{2} \right| \quad (\text{S12})$$

The typical frequency dependence of V_g is shown at Fig. S6. Due to the thermal RC relaxation time, the signal of the sensor attenuates at high frequency. On the other hand, the signal saturates at the DC value at low frequencies. We have measured the frequency dependent read-out signals of the samples and assign the saturated value to determine the thermal conductance of CNTs.

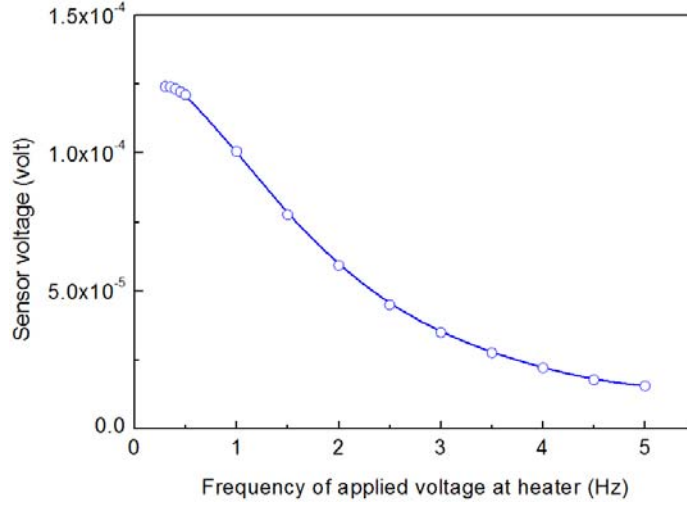


Fig. S6. Measurements of V_g as a function of driving frequency at the heater.

Once V_g is measured, ΔT_s can be obtained using

$$\Delta T_s = \frac{1}{c} \Delta R_s = \frac{1}{c} \left(\frac{\Delta V}{I_{dc}} \right) = \frac{1}{c} \left| \frac{2V_g}{I_{dc}} \right| \quad (\text{S13})$$

where c is the temperature coefficient of R_s .

The noise equivalent thermal conductance (NEK_s) can be evaluated using

$$NEK_s = \frac{NET_s}{\Delta T_h - \Delta T_s} K_b \quad (\text{S14})$$

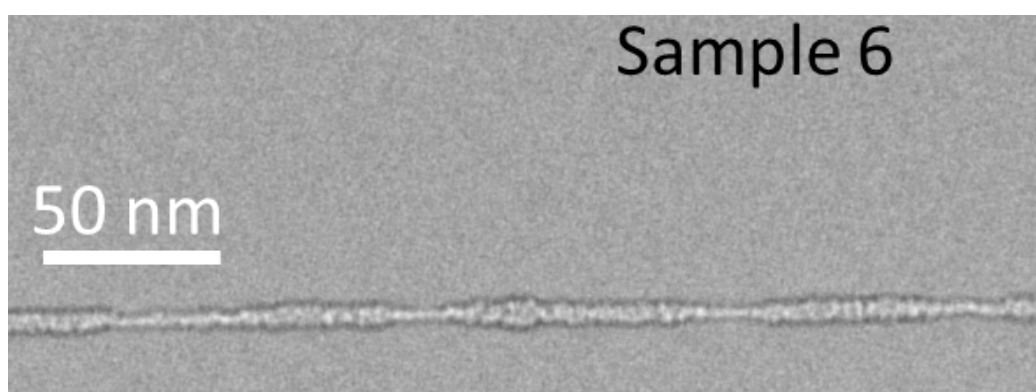
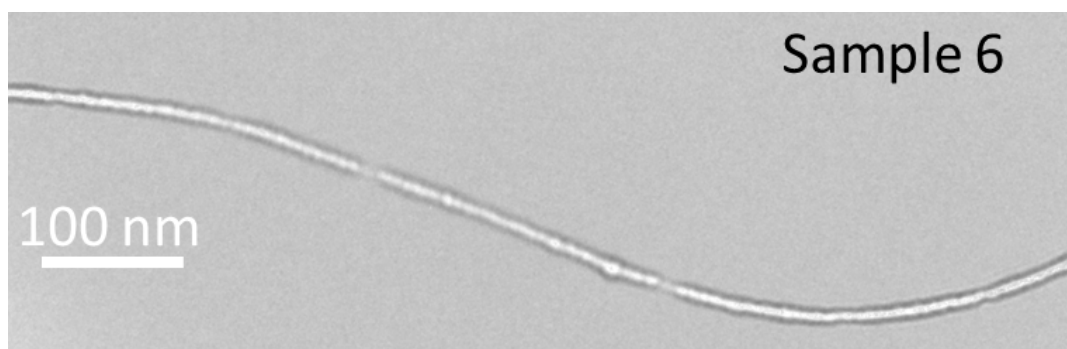
where is NET_s the noise equivalent of ΔT_s , and K_b is the thermal conductance of the beam. From Fig. 1(c) of the main text, we have $NET_s = 0.28\text{mK}$. From Eq. (S4), $K_b = P/2\Delta T_h = 100 \text{ nW/K}$. We obtain $NEK_s = 1.5 \text{ pW/K}$ at room temperature, much better than our previous works [6,7].

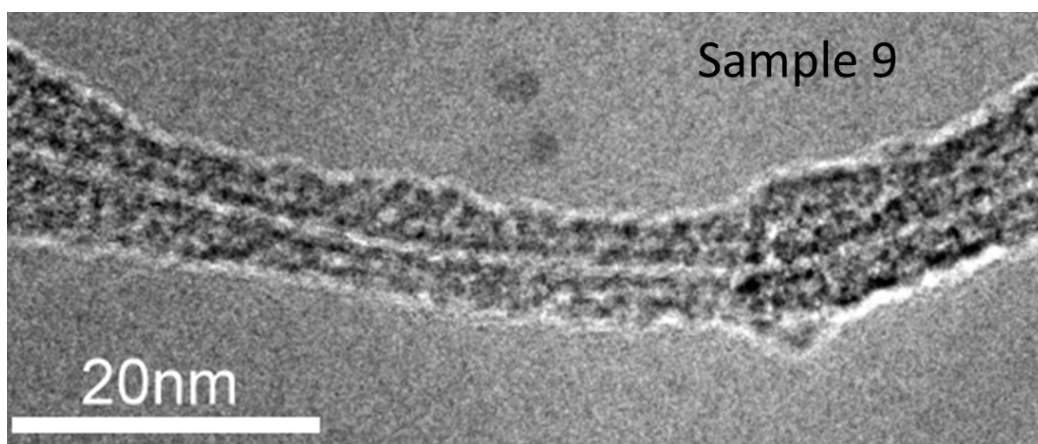
Before measurements on CNTs, we need to subtract the background thermal conductance due to radiation transfer. As shown in Fig 1(d) of the main text, the measured background thermal conductance varies from 3.18×10^{-9} to $4.51 \times 10^{-12} \text{ W/K}$ as the distance of heater to sensor increases from $4\mu\text{m}$ to 1.039mm . In addition, they display symmetric results when exchanging the heater and the sensor. We have found

that the background thermal conductance is sensitive to the environment. For example, devices with fully-etched Si substrates will give smaller background thermal conductance than that of partially-etched Si substrates. Thus the measured background thermal conductance would not be the same even if the heater-to-sensor distances are similar. We have taken special cares to ensure identical experimental environments for each CNT and background measurements.

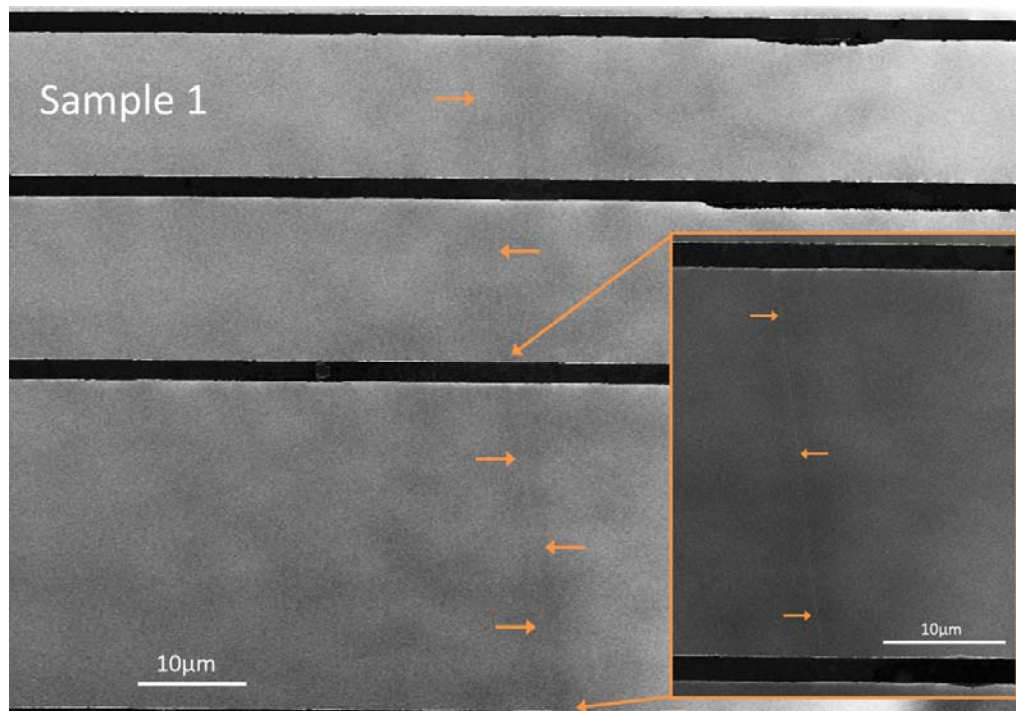
After subtracting the background thermal conductance, the thermal conductivity of the CNT is calculated using $\kappa = KL/A$, where K , L , and A are respectively the thermal conductance, the length of the suspended segment of the CNT between two RT lines, and the cross-sectional area. A is estimated by $A = \pi d\delta$, where $d = 2\text{nm}$ is assumed to be the diameter of the CNT and δ is the conventional thickness (0.34nm) of CNT.

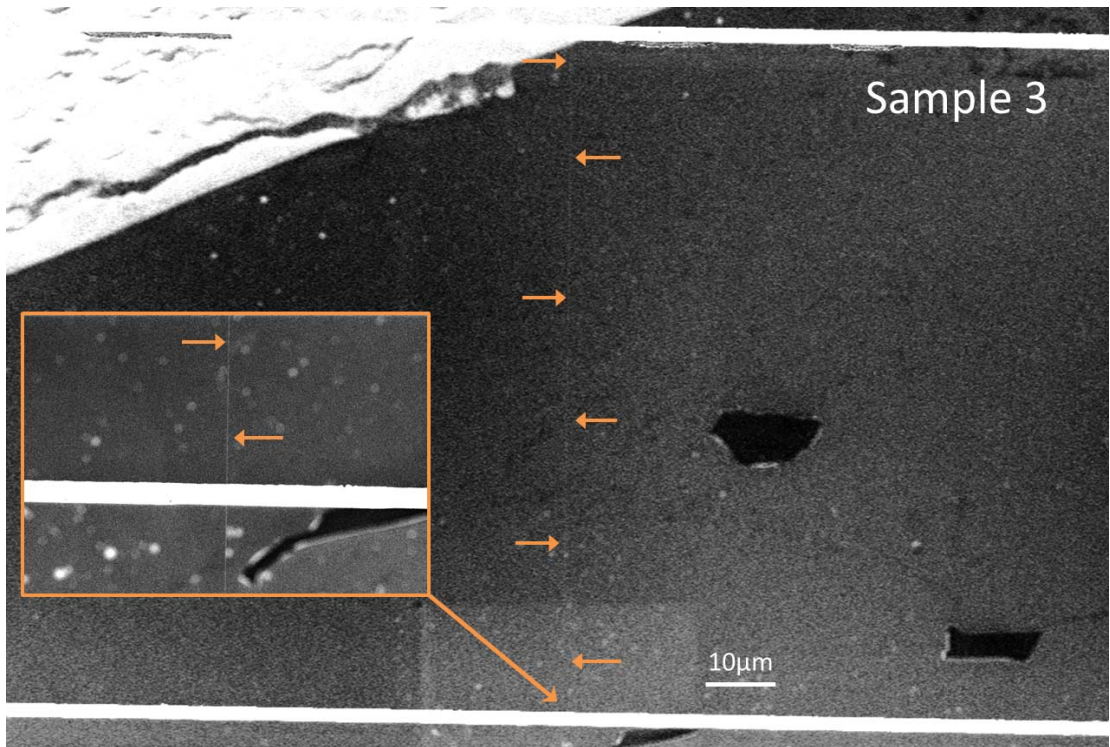
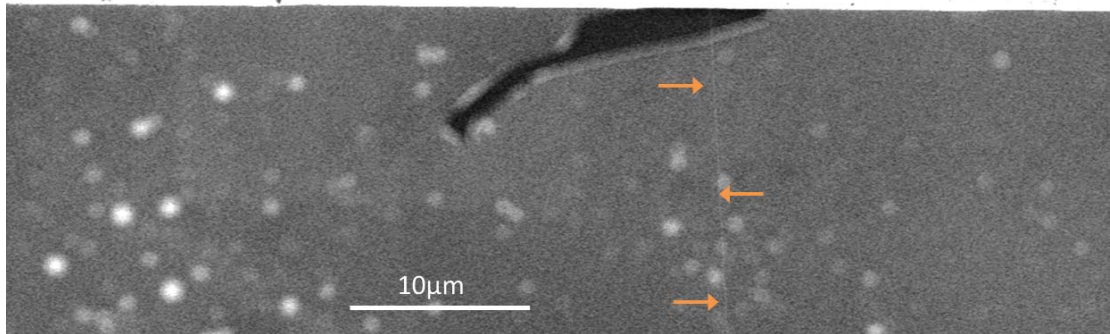
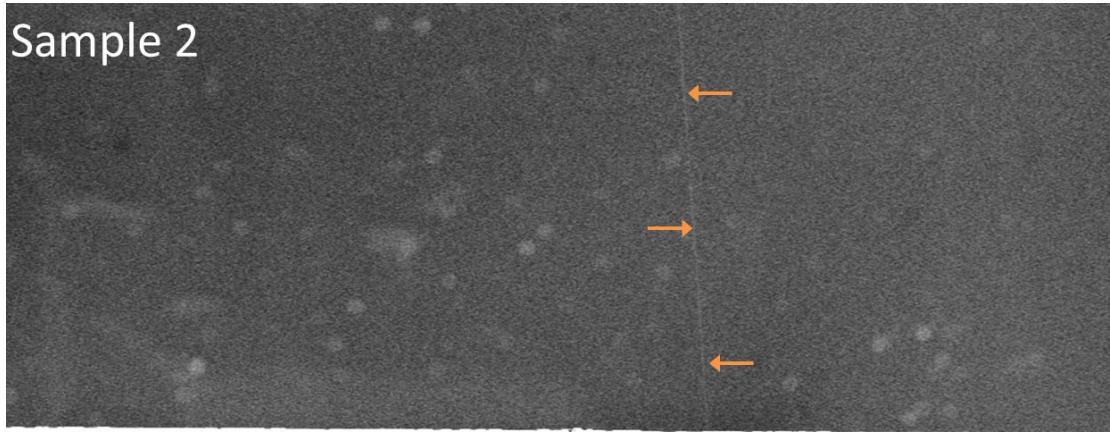
S3. TEM images of the investigated CNTs. After the measurement, sections of Sample 6 and Sample 9 were successfully transferred to a transmission electron microscope (TEM) for further characterizations. Unfortunately, due to mechanical vibrations of the suspended CNTs, their diameters could not be precisely determined. Thus we assume the investigated CNTs exhibit uniform diameter $d = 2\text{nm}$ throughout the paper. Interestingly, the divergent of κ remains even if the TEM images reveal that thin layers of amorphous carbon cover some parts of the investigated CNTs.

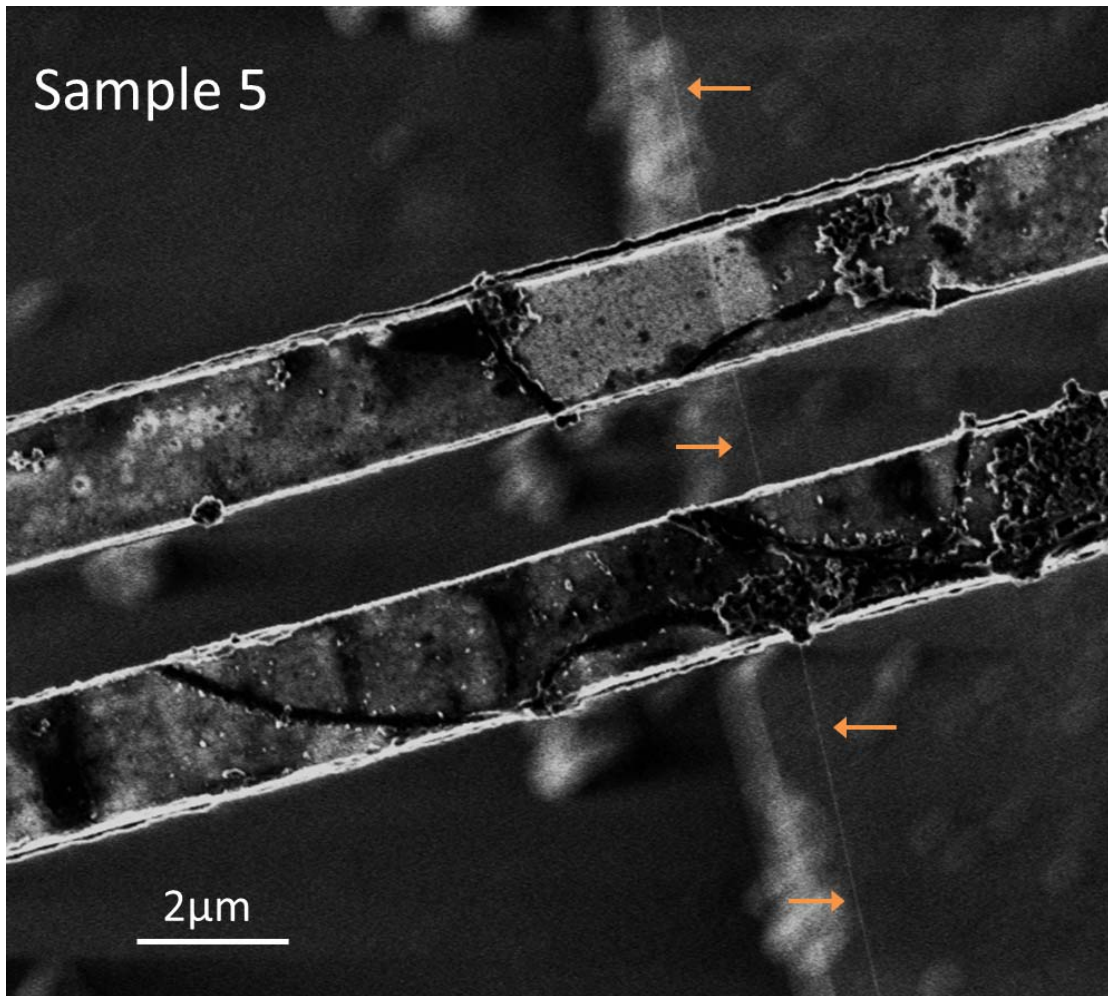
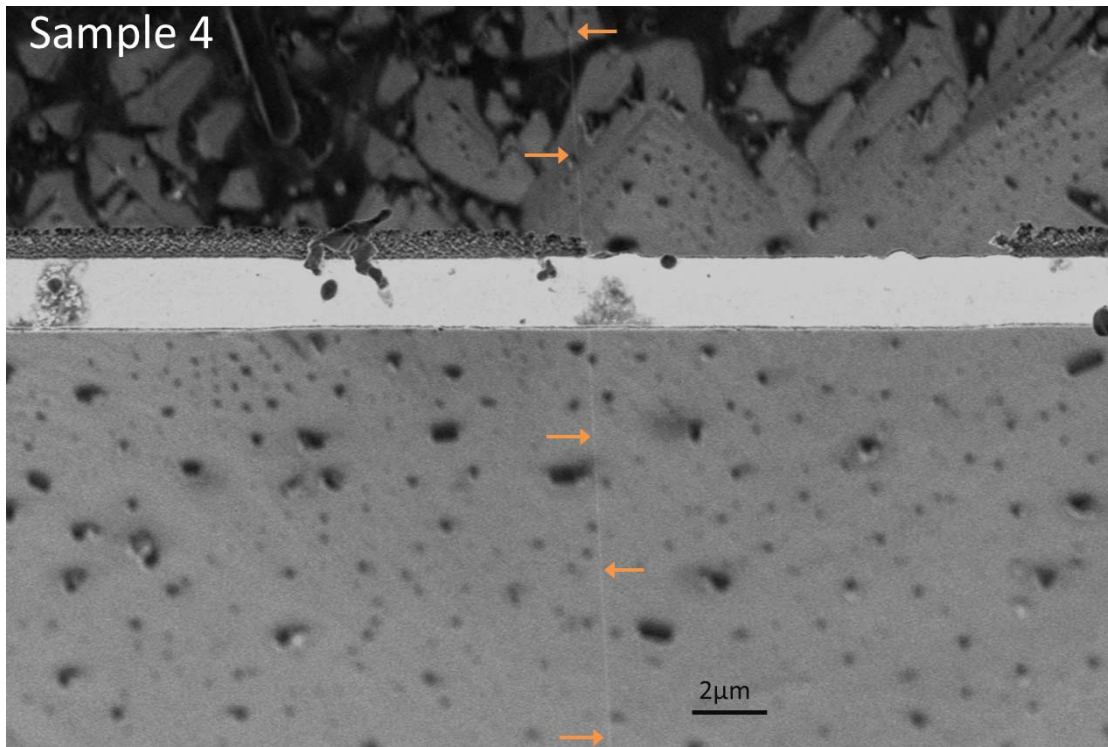


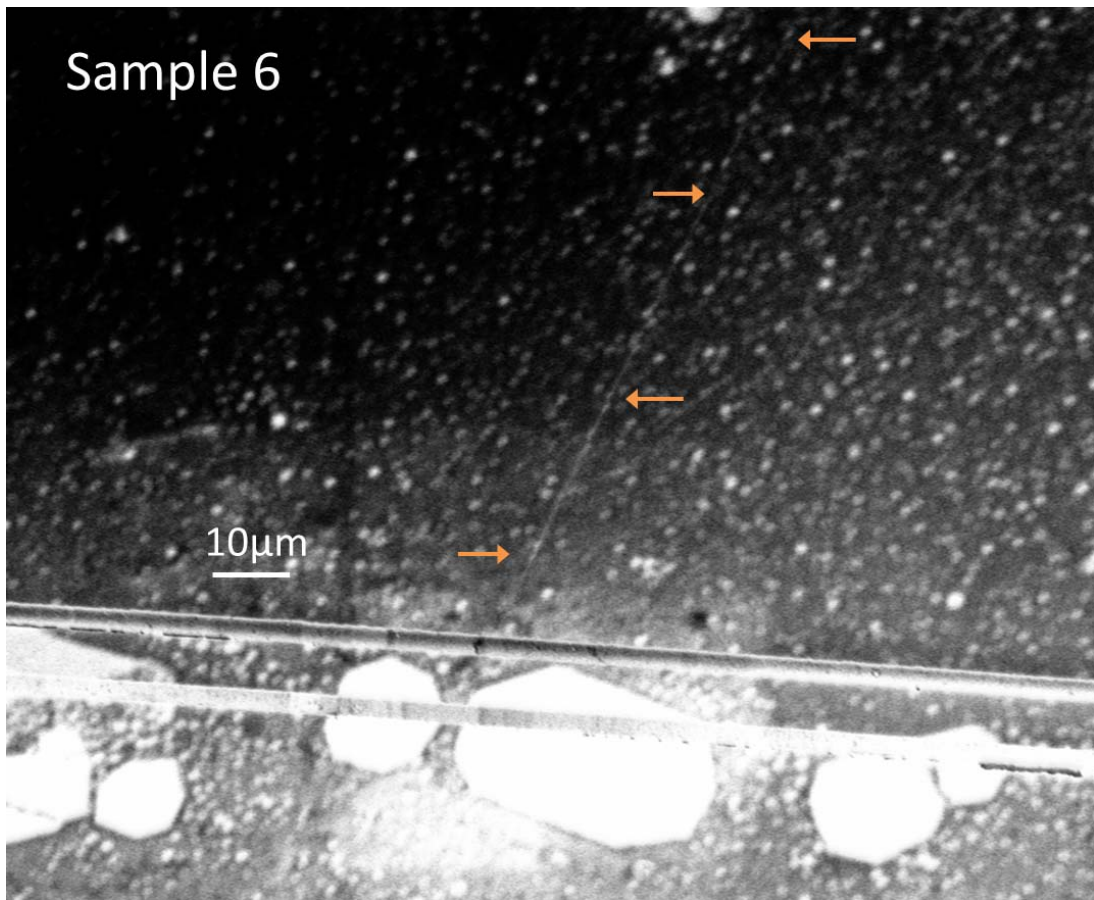
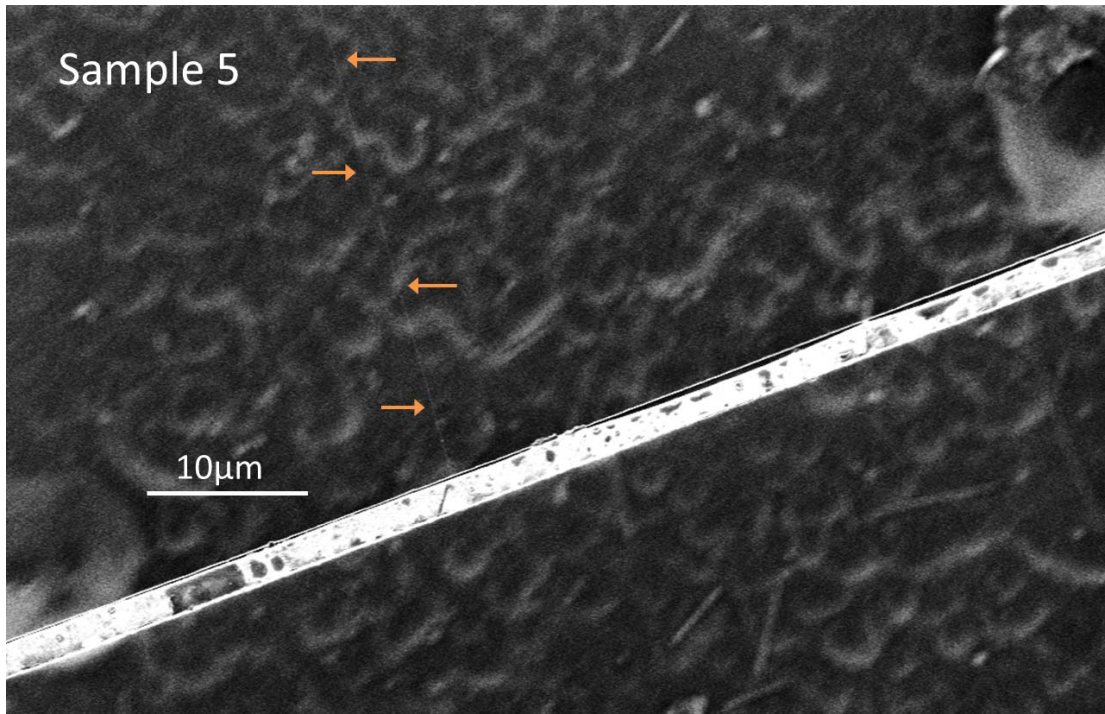


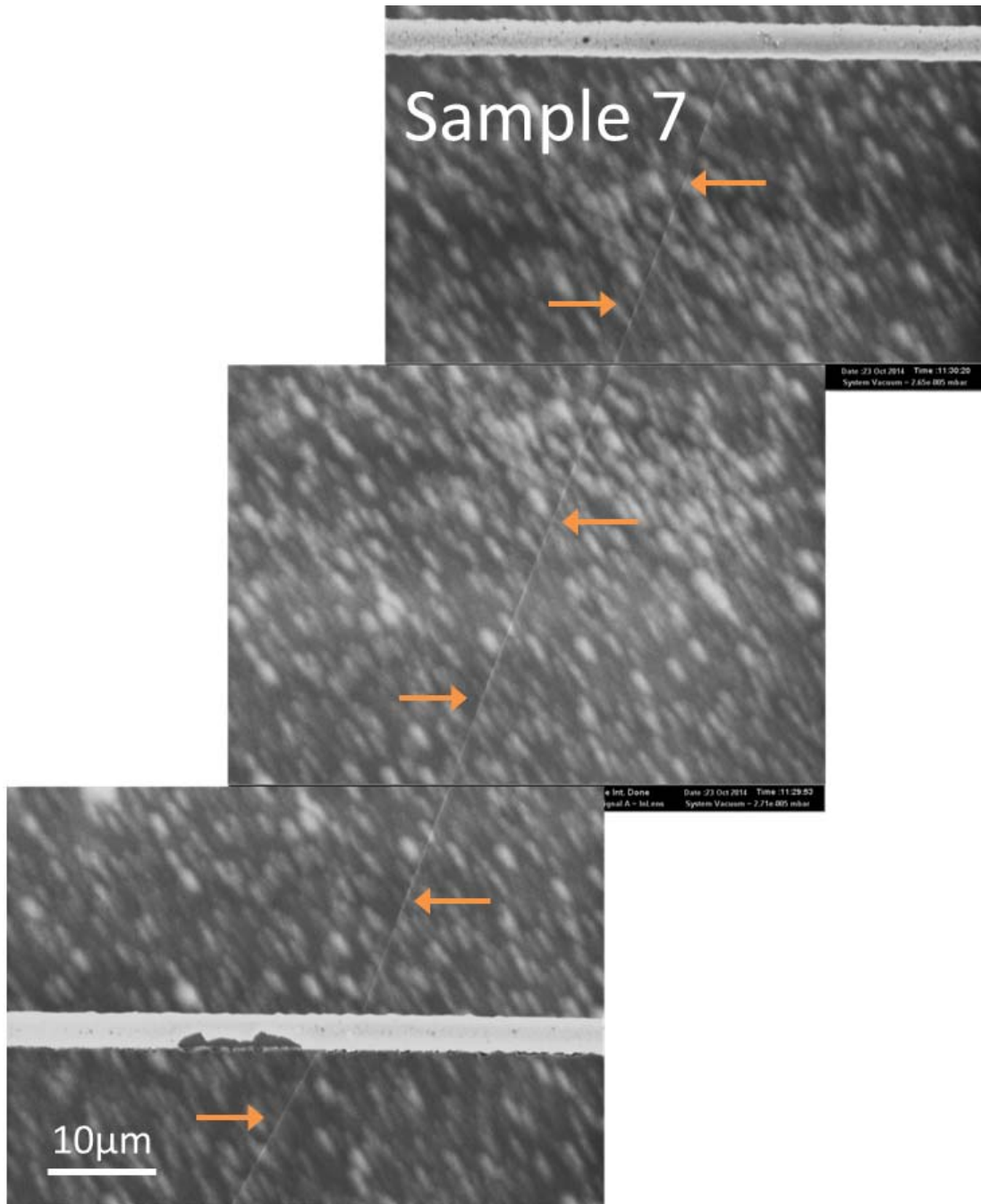
S4. SEM images of the investigated CNTs. The representative SEM images of the measured CNTs are shown below (the arrows denote the location of the CNT).

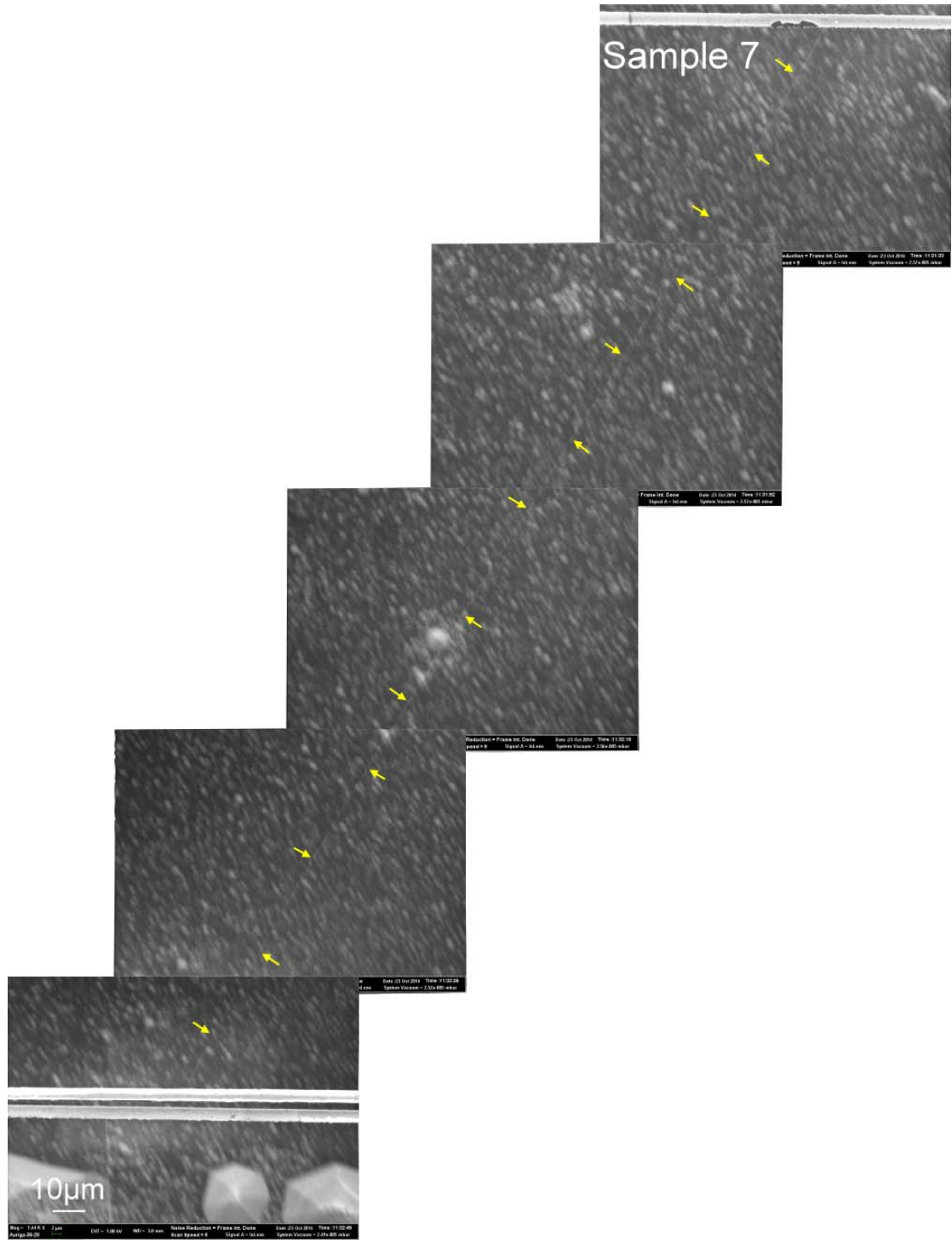


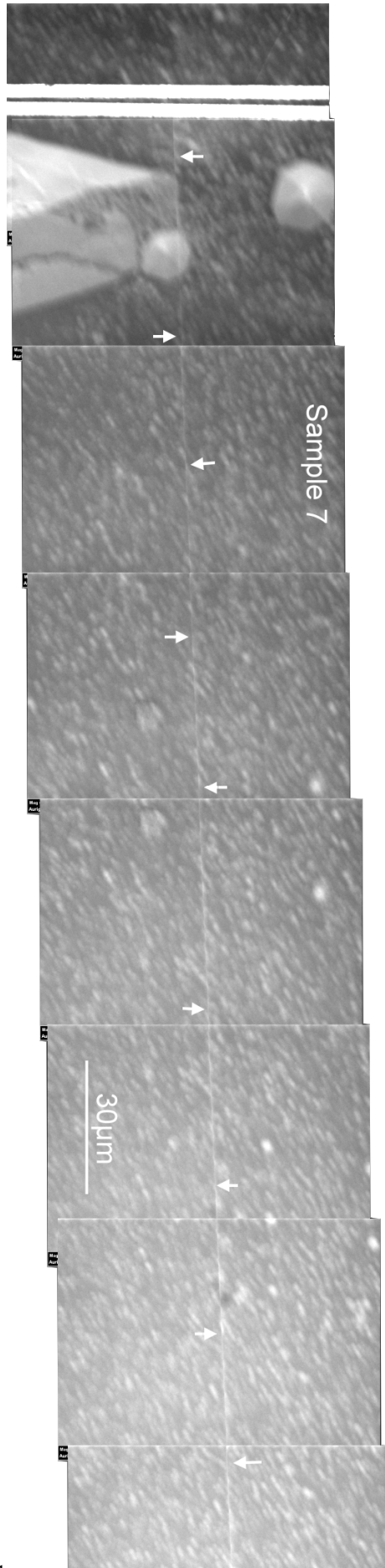
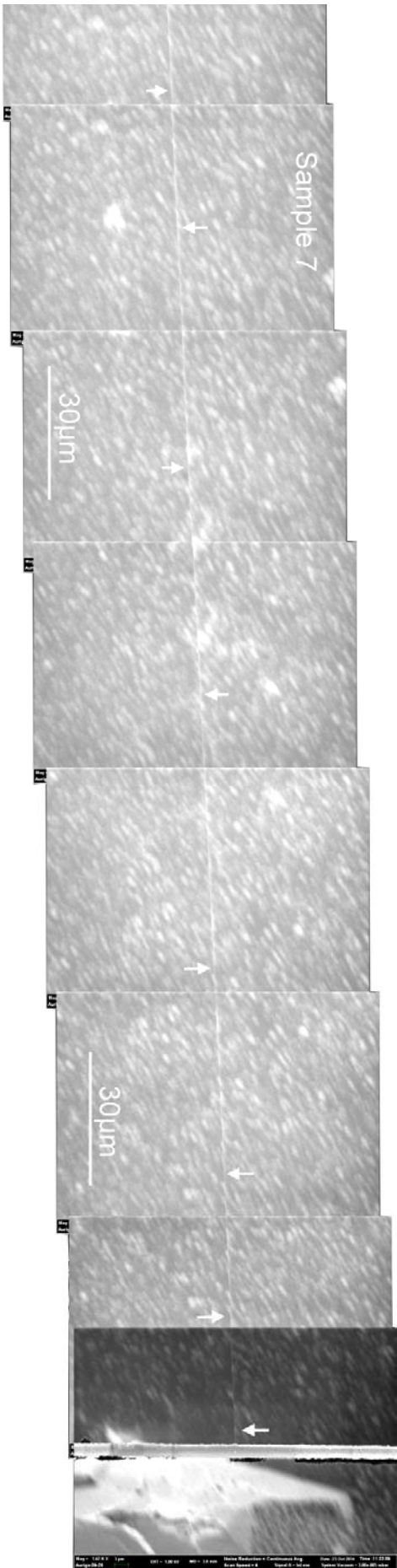


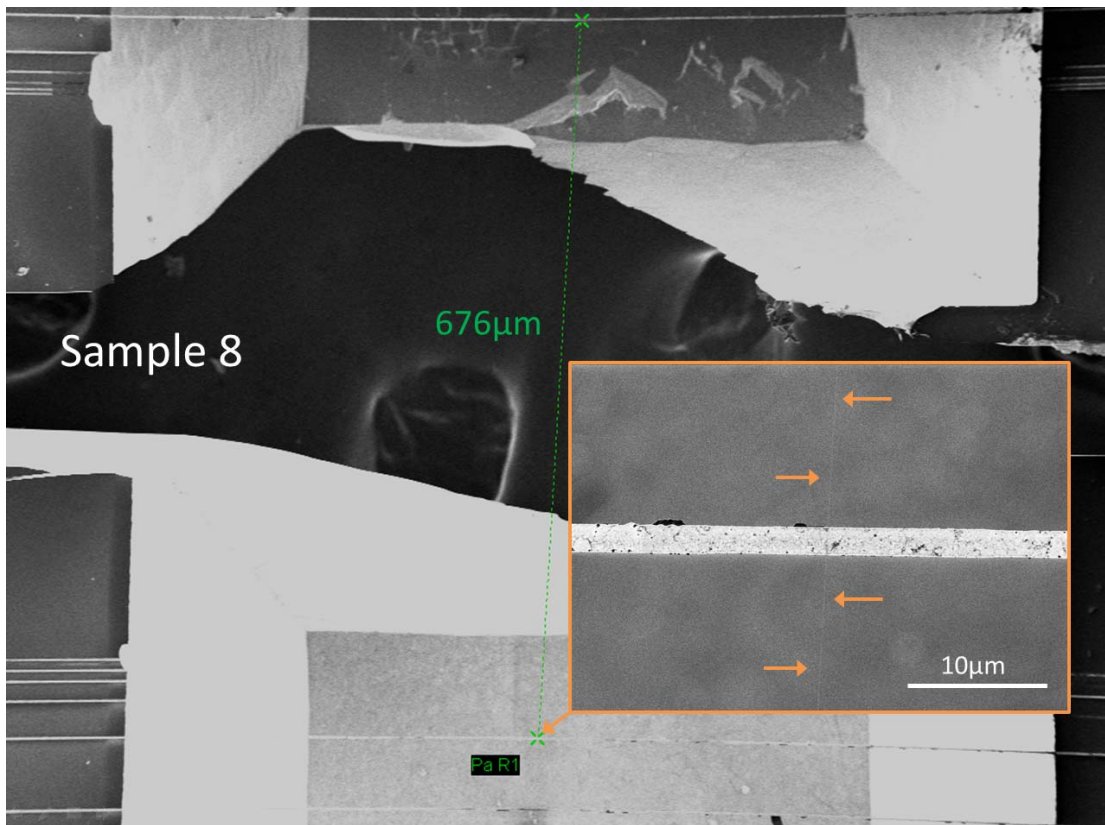
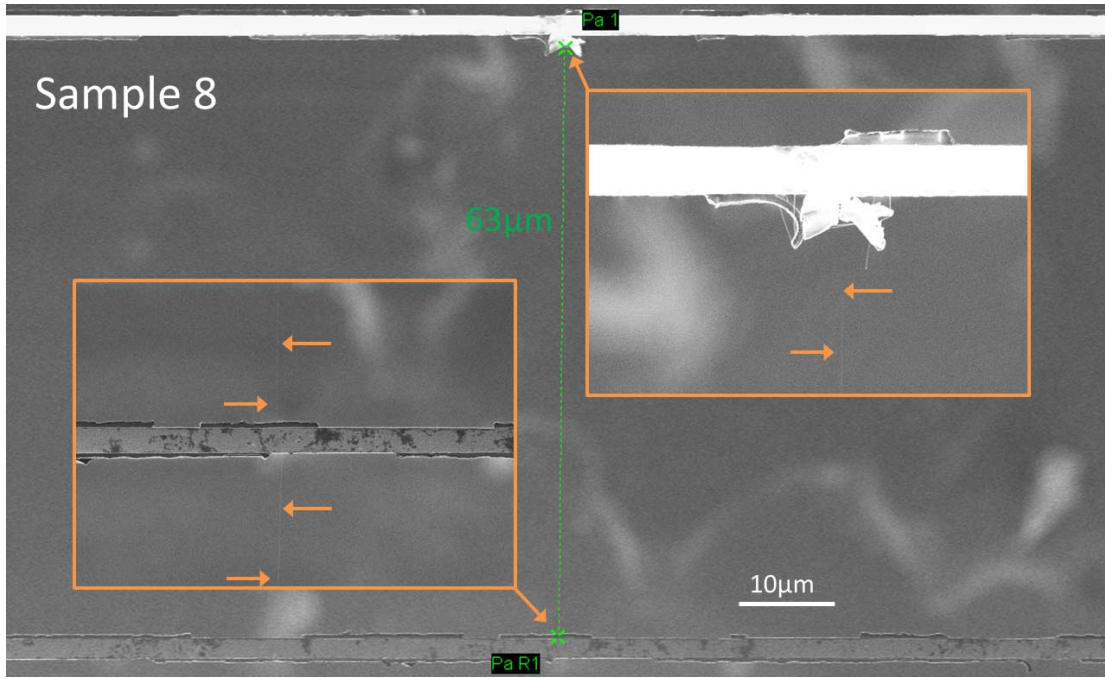


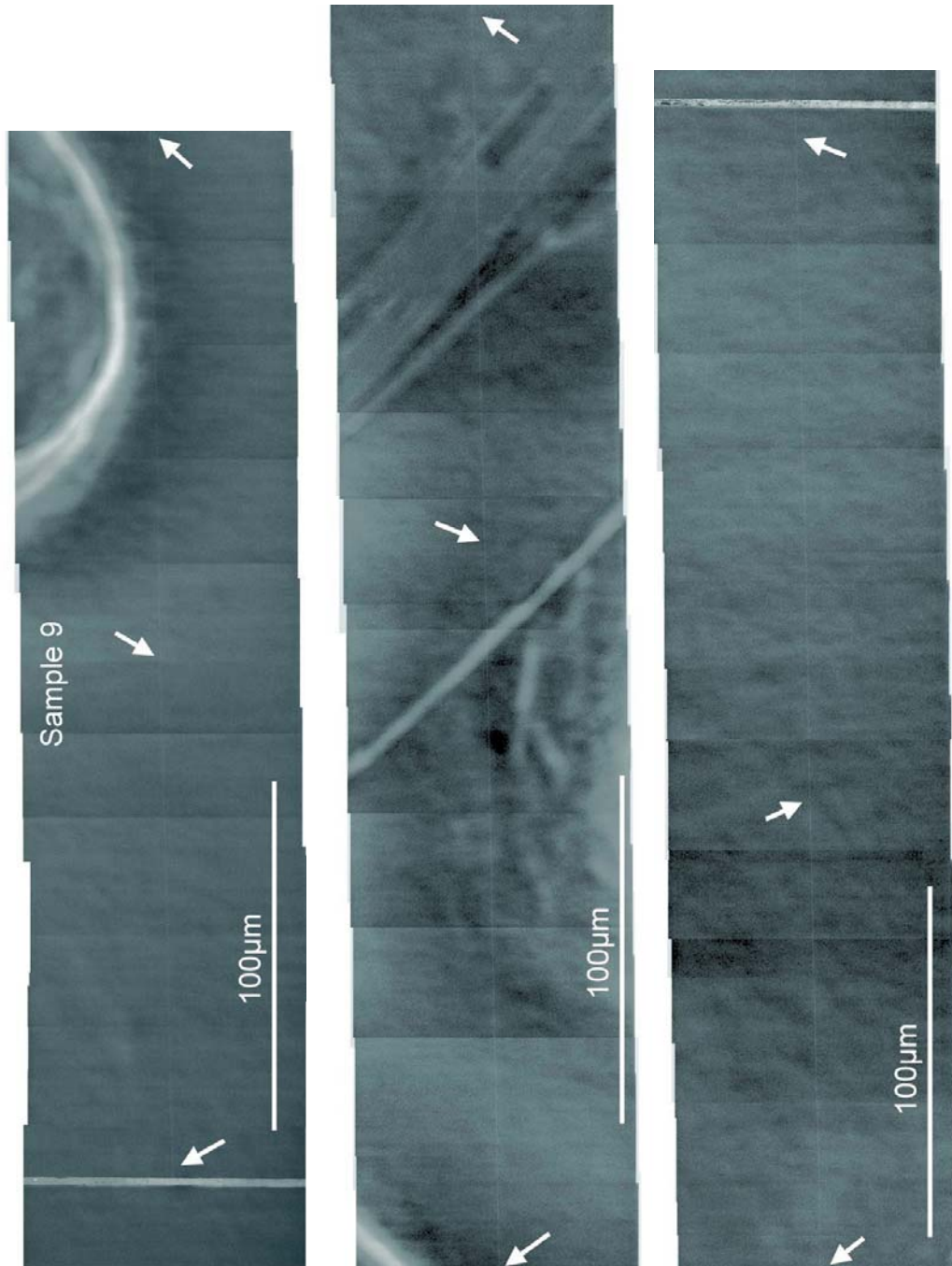












S5. Corrections of thermal radiation from CNT surfaces. Because of thermal radiation from the surface of a CNT, the heat received at the sensor will be always lower than that transmitted from the heater. Thus the measured P underestimates the actual P delivered in the CNT and, correspondingly, the measured K_m simply sets the lower bound of the actual thermal conductance K_s .

The thermal radiation from the CNT surface gives an equivalent thermal resistance (R_r) that can be expressed by:

$$R_r = \frac{T - T_\infty}{\varepsilon \sigma A (T^4 - T_\infty^4)} \quad (\text{S15})$$

where $\varepsilon = 0.98$ is the emissivity of CNT[8], $\sigma = 5.67 \times 10^{-8} \text{ Wm}^{-2}\text{K}^{-4}$ is Stefan-Boltzmann constant, $A = \pi dl$ is surface area of each segment, T is the temperature of the CNT segment, and $T_\infty \sim 300\text{K}$ is the temperature of the environment.

In our experiment, $T - T_\infty < 20\text{K}$, applying the first-order approximation we then have:

$$R_r \approx \frac{1}{4\varepsilon\sigma AT_\infty^3} \quad (\text{S16})$$

The higher-order terms contribute less than 10% of Eq. (S16). Note that although a Fourier thermal conductor exhibits a linear temperature profile along the temperature gradient, the temperature profile for a non-Fourier thermal conductor is unknown. Yet applying the approximation in Eq. (S16) has ignored the uncertainty of the temperature profile along the CNT, which is estimated to contribute less than 10% of the final result. Now we estimate the ratio R_r/R (where R is the thermal resistance of the CNT). Assuming the thermal conductivity of a $1\mu\text{m}$ -long CNT is $\sim 3000 \text{ W/m-K}$ and $\varepsilon = 0.98$, we have

$$\frac{R_r}{R} \approx 2.45 \times 10^5 \quad (\text{S17})$$

The result suggests that thermal radiation is negligibly small for short CNTs. In fact, we estimate that it would give about 1% correction to the measured thermal conductivity for a $30\mu\text{m}$ -long CNT.

However, corrections from thermal radiation will become more significant for ultralong CNTs. To estimate K_s for ultralong CNTs, a thermal circuit model shown in Fig. S7 is employed to correct K_m . Because the maximum thermal conductance of a finite-length CNT is limited by quantum mechanics [9], the CNT of total length L is divided into segments of mean free path (l) in series. Notably, the measured thermal conductivity κ_m will be always lower than the corrected thermal conductivity $\kappa = L/\Sigma R = L/[(L/l)R] = l/R$ for any finite R_r .

Because the temperature profile across a mean free path is uniform, we can determine R_r due to thermal radiation of heat into environment. The thermal resistance of each segment of a CNT is R , as shown in Fig. S7.

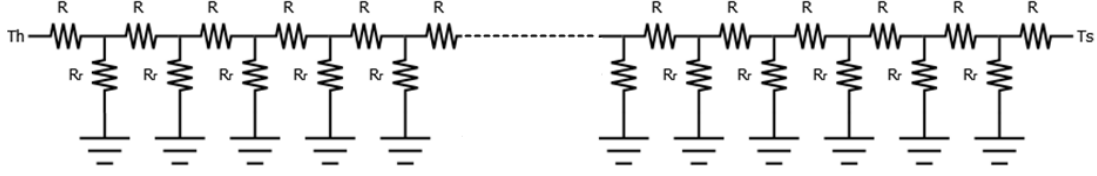


Fig. S7. The thermal circuit model for evaluating the contribution of thermal radiation to the corrected thermal resistance of CNT. Here R is the corrected thermal resistance of each segment of a CNT, and R_r is the equivalent thermal resistance due to thermal radiation for each segment.

We firstly demonstrate that the discrete model correctly converges to continuum results. Assuming the sample is a diffusive thermal conductor (i.e. $l \rightarrow 0$), then the number of segment in the circuit model can be arbitrarily increased. As shown in Fig. S8, for a sample with $\kappa = 1500$ W/m-K and $L = 400\mu\text{m}$, the model quickly converges to $\kappa/\kappa_m = 150\%$ when the number of segments increases beyond 10. The result justifies the discreteness of the circuit model since the numbers of segments in the following discussions are always much larger than 10.

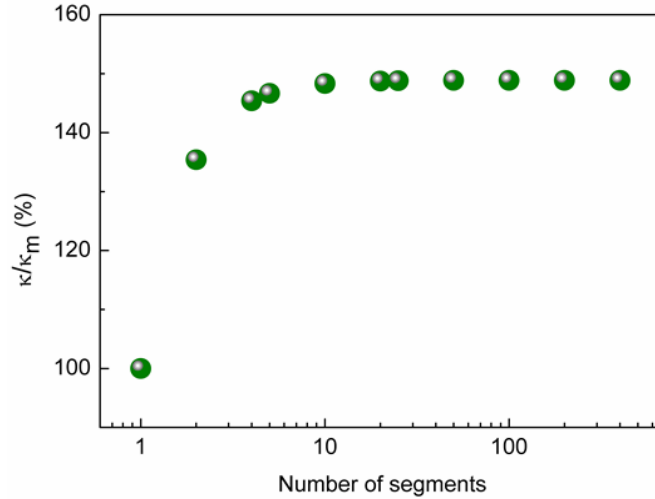


Fig. S8. The ratio of corrected thermal conductivity to measured thermal conductivity (κ/κ_m) as a function of segment in the circuit model. Here the sample is assumed to be a diffusive thermal conductor with $\kappa_m = 1500$ W/m-K and $L = 400\mu\text{m}$. The correction quickly converge to $\kappa/\kappa_m = 150\%$ when the number of segment is larger than 10. The result justifies the discrete thermal circuit model.

We then apply the analyses to samples of different κ_m 's and L 's (because both R_r and R inversely depend on the diameter d , the correction is independent of d). The result is shown in Fig. S9. As expected, the correction of thermal radiation to κ_m becomes more significant for large L 's.

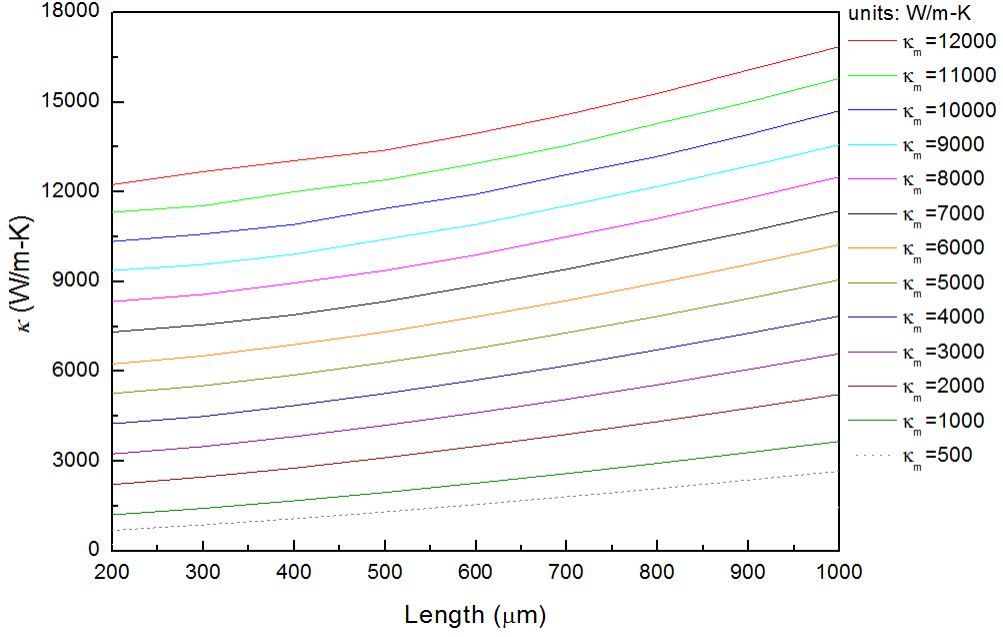


Fig. S9. Corrected thermal conductivity (κ) as a function of length (L) for different measured thermal conductivity (κ_m). Because of the larger heat loss via thermal radiation from CNT surfaces, the correction becomes more pronounced for longer L 's.

The above results are based on the practical assumption that the thermal resistance of a $1\mu\text{m}$ -long CNT is $R_{1\mu\text{m}} = 1.56 \times 10^8 \text{ K/W}$ (which corresponds to thermal conductivity 3000 W/m-K). Although the assumption is close to the theoretical limit, the R may vary as the CNTs' quality changes. Indeed, the $R_{1\mu\text{m}}$ could increase due to the presence of impurities or defects. To estimate the effect on our analyses on thermal radiation, we plotted the κ/κ_m when $R_{1\mu\text{m}}$ changes (here we set $L = 400\mu\text{m}$ as an example). As shown in Fig. S10, for a given κ_m , changing $R_{1\mu\text{m}}$ can hardly change κ/κ_m . It is because for a sufficiently long CNT, the ratio of L/l is much larger than 10, and thus changing the number of segments in the thermal circuit model cannot affect the correction on κ .

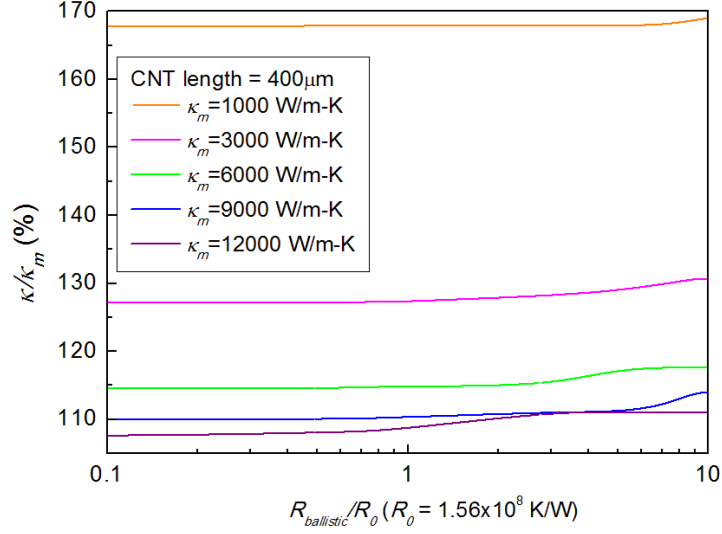


Fig. S10. The ratio of corrected thermal conductivity to measured thermal conductivity (κ/κ_m) for different input $R_{1\mu\text{m}}$. It can be seen that for a sufficiently long CNT (here $L = 400\mu\text{m}$), changing $R_{1\mu\text{m}}$ can barely affect the κ/κ_m .

S6. Thermal conductivity data of the investigated CNTs. The experimental data of the investigated CNTs are summarized in Table S1 (assuming $d = 2\text{nm}$ and $\delta = 0.34\text{nm}$).

Table S1. Measured K_m , κ_m , corrected κ (after radiation correction), and the corresponding background thermal conductance (K_{bg}) for the investigated CNTs.

	$L(\mu\text{m})$	K_m (pW/K)	κ_m (W/m-K)	κ (W/m-K)	K_{bg} (pW/K)
Sample 1	2	2932±50	2747±47	2747±47	16500±19
	15.7	352±5.7	2587±42	2587±42	456±2.9
	31.5	190±6.9	2806±102	2867±87	185±1.6
Sample 2	3.9	1140±13	2082±24	2082±24	3181±5.9
	7.7	764±7.8	2757±28	2757±28	835±5.0
	15.5	397±6.1	2879±44	2879±44	298±3.2
	96.2	83±8.6	3738±387	3800±417	47.7±3.5
	126	73±14.8	4332±873	4447±910	40.5±5.8
Sample 3	4	1442±18	2701±34	2701±34	3181±8.9
	7.8	729±10	2665±37	2665±37	835±6.0
	15.4	340±8.0	2454±58	2454±58	298±3.2
	96.8	86.3±11.8	3915±537	4021±551	47.7±3.5
	125.6	79±19.8	4648±1165	4737±1170	40.5±5.8
Sample 4	15	391±6.4	2745±45	2745±45	442±4.7
	31	266±9.9	3867±144	3960±84	198±5.2

	190.9	66.2±13.2	5915±1179	6165±1182	20.2±2.8
Sample 5	2	2731±62	2559±58	2559±58	5586±7.7
	300	45.7±1.3	6424±186	6929±213	22.9±0.4
Sample 6	7	153±7.6	502±25	502±25	1542±5.6
	200	14.5±5.9	1363±549	2151±791	54.9±2.2
	400	9.3±2.2	1737±403	2837±194	15.9±1.1
Sample 7	50	51.8±2.5	1212±59	1212±59	436±1.8
	200	19.2±4.9	1803±465	2026±475	53.2±3.8
	400	15.1±4.9	2823±911	3627±955	17.1±3.6
Sample 8	62.8	108±1.9	3169±55	3194±55	240.8±0.7
	676	24.7±2.2	7821±681	10138±706	7.59±0.4
Sample 9	31.2	254±1.2	3717±18	3798±77	437±0.8
	62.8	141±2.0	4148±60	4248±48	237±1.2
	1039	17.7±1.5	8638±734	13471±841	4.56±0.7

S7. Effects of contact thermal resistance. As discussed in the main text, the effect of contact thermal resistance can be analyzed by parametrizing K_s/K_c , where K_s is the thermal conductance of a $1\mu\text{m}$ -long CNT and $1/K_c$ is the contact thermal resistance between the CNT and each RT_i beam. So the measured thermal resistance ($1/K_m$) follows: $1/K_m = (L/L_0)^{1-\alpha}/K_s + 1/K_c$, and the measured κ_m is expressed as:

$$\kappa_m = \frac{K_s L}{\pi d \delta} \left(\frac{1}{(L/L_0)^{1-\alpha} + K_s/K_c} \right) \quad (\text{S18})$$

here $L_0 = 1\mu\text{m}$. We have excluded the possibility that contact thermal resistance could give spurious divergent behavior for a diffusive thermal conductor (i.e. $\alpha = 0$) in Fig. 4 of the main text. Now we further analyze the data for $\alpha > 0$.

From Fig. S11, we see that only when $0.17 < \alpha < 0.43$ and $K_s/K_c < 0.3$ can the calculated curves fit the experimental data well (excluding Sample 1). The results give additional supports that the observed phenomena are due to the anomalous thermal conduction in CNTs but not experimental artifacts.

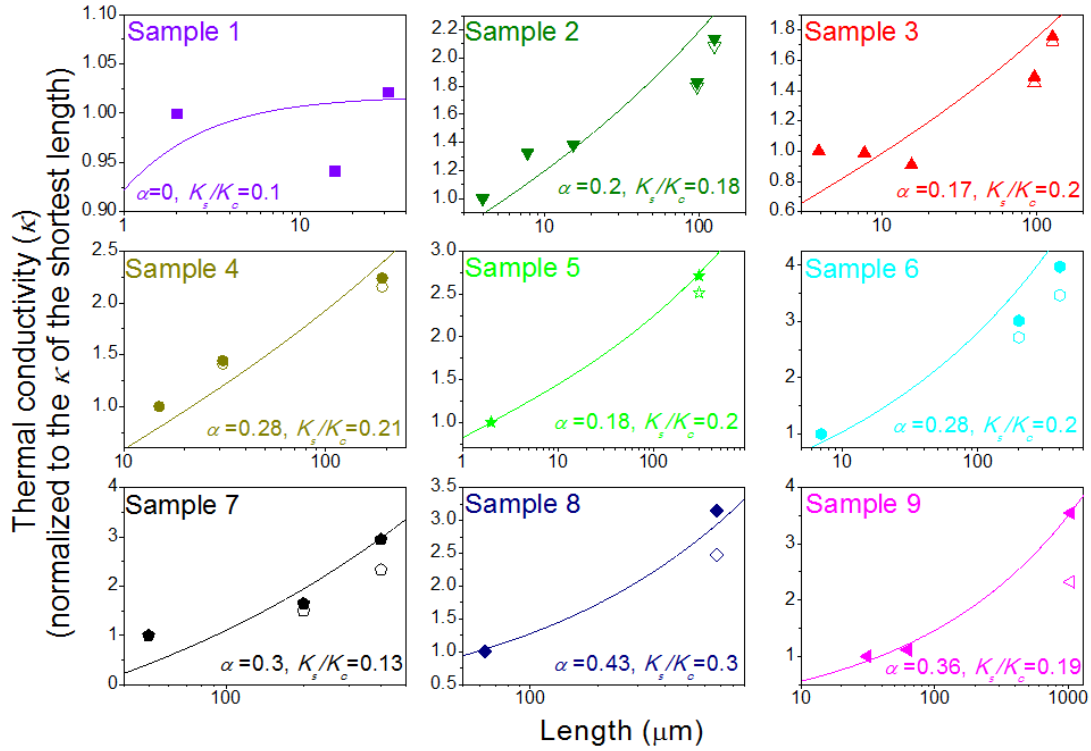


Fig. S11. Data fitting for the corrected thermal conductivity (κ) using α and K_s/K_c (open symbols are measured thermal conductivity (κ_m)). Except for Sample 1, it can be seen that only when $0.17 < \alpha < 0.43$ and $K_s/K_c < 0.3$ can the calculated curves fit well to the experimental data.

References

- [1] M. Hofmann, D. Nezich, A. Reina, and J. Kong. *Nano Lett.* **8**, 4122 (2008).
- [2] B. H. Hong, J. Y. Lee, T. Beetz, Y. M. Zhu, P. Kim, and K. S. Kim. *J. Am. Chem. Soc.* **127**, 15336 (2005).
- [3] S. M. Huang, X. Y. Cai, and J. Liu. *J. Am. Chem. Soc.* **125**, 5636 (2003).
- [4] L. X. Zheng, M. J. O'Connell, S. K. Doorn, X. Z. Liao, Y. H. Zhao, E. A. Akhadorov, M. A. Hoffbauer, B. J. Roop, Q. X. Jia, R. C. Dye, D. E. Peterson, S. M. Huang, J. Liu, and Y. T. Zhu. *Nat. Mater.* **3**, 673 (2004).
- [5] T. L. Bergman, A. S. Lavine, and F. P. Incropera. *Fundamentals of Heat and Mass Transfer*. 7th edn, (Wiley, 2011).
- [6] T. K. Hsiao, H. K. Chang, S. C. Liou, M. W. Chu, S. C. Lee, and C. W. Chang. *Nature Nanotech.* **8**, 534 (2013).
- [7] T. K. Hsiao, B. W. Huang, H. K. Chang, S. C. Liou, M. W. Chu, S. C. Lee, and C. W. Chang. *Phys. Rev. B* **91**, 035406 (2015).
- [8] R. Fainchtein, D. M. Brown, K. M. Siegrist, A. H. Monica, E. R. Hwang, S. D. Milner, and C. C. Davis. *Phys. Rev. B* **85**, 125432 (2012).
- [9] N. Mingo and D. A. Broido. *Phys. Rev. Lett.* **95**, 096105 (2005).